ARMY RESEARCH LABORATORY

Hot Explosive Consolidation of W-Ti Alloys: Microstructural Effects

by Laszlo J. Kecskes

ARL-TR-2615 November 2001

NOTICES

Disclaimers

The findings in this report are not to be construed as an official Department of the Army position unless so designated by other authorized documents.

Citation of manufacturer's or trade names does not constitute an official endorsement or approval of the use thereof.

Destroy this report when it is no longer needed. Do not return it to the originator.

Army Research Laboratory
Aberdeen Proving Ground, MD 21005-5069

ARL-TR-2615 **November 2001**

Hot Explosive Consolidation of W-Ti Alloys: Microstructural Effects

Laszlo J. Kecskes
Weapons and Materials Research Directorate, ARL

Abstract

Full-density W-Ti alloys have been fabricated by a recently developed, hot-explosive-compaction (HEC) technique. The alloy billets, which are formed, consist of W grains embedded in a generally discontinuous, preferentially oriented Ti-rich matrix. The effects of the use of different types of precursor powders, the influence of the W-Ti ratio on the dispersability of the W grains in the alloy, and the postconsolidation anneal control of the Ti-rich matrix were of primary interest. The alloy billets were analyzed by X-ray diffraction (XRD), scanning electron microscopy (SEM), and energy dispersive spectroscopy (EDS). The major features of the technique and the microstructural properties of the W-Ti alloys are presented.

Contents

List of Figures v

List of Tables vii

1. Introduction 1

2. Experimental Procedure 3

2.1 Billet Preparation and Fabrication Procedure 3

2.2 Sample Characterization 5

2.3 W Powder Coating Experiments 7

2.4 Post-Consolidation Annealing Treatments 8

3. Results and Discussion 9

3.1 Size Control of the Matrix 9

3.2 Effect of the W:Ti Ratio on the Matrix 11

3.3 Coated W Powder Effects of the Matrix 22

3.4 Post-Consolidation Anneal Control of the Matrix 23

4. Conclusions 27

5. References 29

Appendix. Temperature History and Microstructure Evolution of the CSA-HEC Samples 31

Distribution List 41

Report Documentation Page 43

INTENTIONALLY LEFT BLANK.

List of Figures

Figure 1(a). CSA-HEC method: (a) schematic diagram of the apparatus. 4

Figure 1(b). CSA-HEC method: (b) precompaction temperature history of the W+Ti powder bed 6

Figure 2. Schematic diagram of the PVD/DC sputtering system that was used to fabricate the Ti-coated W powder. 8

Figure 3. BSE-COMP micrographs of core regions of the 83W-17Ti alloys: (a) standard, (b) coarse, and (c) fine. 10

Figure 4. BSE-COMP micrographs of the alloys: (a) unalloyed W, (b) 83W-17Ti, (c) 70W-30Ti, (d) 60W-40Ti, (e) 51W-49Ti, and (f) unalloyed Ti. 12

Figure 5. XRD scans of the CSA-HEC sample cores: (a) unalloyed W, (b) 83W–17Ti, (c) 70W–30Ti, (d) 60W–40Ti, (e) 51W–49Ti, and (f) unalloyed Ti. 14

Figure 6. XRD scans of the CSA-HEC sample edges: (a) unalloyed W, (b) 83W–17Ti, (c) 70W–30Ti, (d) 60W–40Ti, (e) 51W–49Ti, and (f) unalloyed Ti. 17

Figure 7. W-Ti equilibrium phase diagram. 21

Figure 8. BSE-COMP micrographs of the core regions of W-Ti alloys fabricated from Ti-coated W powder: (a) 0.19 Ti atomic-percent, (b) 0.50 Ti atomic-percent, (c) 1.14 Ti atomic-percent, and (d) 2.67 atomic-percent Ti. 24

Figure 9. BSE-COMP micrographs of substructures forming during annealing: (a) 700 °C, (b) 1,000 °C, and (c) 1,400 °C. 25

Figure A-1. Temperature data for the 83W-17Ti powder bed with an $n_{TiC}/n_s = 3.20$ is shown in (a), $n_{TiC}/n_s = 6.29$ is shown in (b), $n_{TiC}/n_s = 9.07$ is shown in (c), and interior temperature for all three n_{TiC}/n_ss is shown in (d). 32

Figure A-2. BSE-COMP micrographs of polished surfaces of a typical 83W-17Ti billet. Core region is shown in (a), transition region is shown in (b), and edge region is shown in (c). 37

INTENTIONALLY LEFT BLANK.

List of Tables

Table 1. Precursor size effect on density. 9
Table 2. W:Ti ratio effects on density and microhardness. 11
Table 3. Annealing temperature effect on microhardness; 83W-17Ti. 27

INTENTIONALLY LEFT BLANK.

1. Introduction

The development of improved W alloys is of continued interest in the U.S. Army's long-rod kinetic energy penetrator program. Novel fabrication techniques are being explored for the production of a new class of two-phase W alloys with a binder (matrix) phase (such as Ti) susceptible to failure by shear localization. The requirements for these alloys are high density, high strength, high hardness, and moderate ductility. A typical morphology envisions uniformly dispersed W grains in the matrix, wherein the amount of binder is minimized without a compromise of the aforementioned properties. In response, a new explosive compaction technique has been developed for W-Ti alloys at the U.S. Army Research Laboratory (ARL).

Over the past three decades, explosive compaction has been applied to a variety of metal and ceramic powders [1, 2]. However, due to the rapid densification rate, the samples often suffer from low, nonuniform densities, poor interparticle bonding, and severe cracking. The temperature rise associated with the irreversible work occurring during the collapse of powders has frequently been found to be insufficient for adequate bonding to develop. Hot explosive compaction (HEC) has been suggested as a way to reduce these problems [3, 4] and has been examined by other investigators [5–8]. The main advantage of preheating the powder is to decrease its yield strength, thereby increasing ductility, and to achieve greater thermal softening.

At ARL, a variant of HEC has been applied to the consolidation of W-Ti alloys. In this technique, referred to hereafter as combustion synthesis assisted HEC (CSA-HEC), an in-situ Ti+C self-propagating high-temperature synthesis (SHS) reaction (i.e., chemical furnace) is used to preheat the powder prior to compaction. Chemical heating is not new [9], and thermite mixtures have been used [10] to heat samples prior to shock loading. Likewise, admixed exothermic mixtures have also been shock initiated to locally enhance sample properties [7, 8].

The chemical furnace is a highly exothermic mixture of reactant powders, which, when ignited, will generate heat and high temperatures. Such reactions can be included under the broader classification of combustion synthesis or SHS reactions. SHS has been extensively researched in the former Soviet Union, Japan, and the United States [11, 12].

A significant difference between CSA-HEC and competing processing methods, such as liquid-phase sintering or conventional HEC, is that in the former, the material to be compacted remains at high temperatures for only a short time. In CSA-HEC, the short preheating cycle is followed by a rapid temperature quench

during densification. These characteristics are critical if properties, such as mechanical strength, size distribution, and morphology of the refractory precursor, are to be retained. The rapid cooldown may also reduce impurity segregation at interfaces or grain boundaries. Control of the available heat and peak temperature achieved during preheating can limit the amount of sintering, dissolution, and melting in each phase to maintain the precursor structure and morphology.

Conventional HEC has been limited to homogeneous systems, such as pure and prealloyed metals and ceramic powders. An extension of HEC to the W-Ti binary alloy system would allow the dissolution of W into the Ti matrix. During the quench following consolidation, the resultant solid solution would likely be retained. In CSA-HEC, the duration of the heating phase is greatly reduced; therefore, solid solution formation would be limited, leaving the precursor W grain morphology mostly intact.

The initial effort at ARL focused on the moderately high-density (16.55g/cm^3) 83W-17Ti atomic-percent (95-5Ti weight-percent) alloy system [13]. The full-density (98%+ theoretical density [TD]), disk-shaped CSA-HEC alloy billets could be divided into an annular periphery and an inner core. In the edge region, most of the W particles had dissolved. The resultant structure consisted of W particle remnants in a primarily W-rich matrix. In contrast, the core region of the disk consisted of W particle agglomerates surrounded by a partially continuous Ti-rich matrix. The lack of continuity or incomplete dispersion of Ti in the billet resulted from the considerable size difference of the precursors, their relative melting points, and the temperature at the time of compaction.

Radial and axial cross sections of the billets (with respect to the compaction axis) revealed an isotropic distribution of the primary and secondary phases in the radial plane; however, both phases were elongated in the axial plane. The nonuniform elongation of the Ti-rich matrix regions arose during the uniaxial collapse of the initially isotropic W+Ti powder bed. The heterogeneity and spatial dependence of the matrix, especially near the periphery, were determined by the precompaction temperature history of the W+Ti powder bed. An expanded description of the temperature history and resultant microstructures are provided in the Appendix.

The following is an account of the efforts designed to modify the CSA-HEC billet structure. The effects of the use of different precursor powders and the variation of the W:Ti ratio (dilution) on the alloying and dispersability of the W grains in the billet were examined. Concurrent with better precursor size matching and dilution, another approach was attempted to improve the uniformity of the matrix phase. It was postulated that only W, coated with a thin Ti layer, would ensure a uniform billet structure. Hence, experiments were conducted with Ti deposited onto the precursor W particles and the coated powder was consolidated by CSA-HEC. Finally, the postconsolidation anneal control of the

Ti-matrix was studied. The alloy billets were analyzed by x-ray diffraction (XRD), scanning electron microscopy (SEM), energy dispersive spectroscopy (EDS), and microhardness measurements. The major features of the resultant properties of the W-Ti alloys are herein described.

2. Experimental Procedure

2.1 Billet Preparation and Fabrication Procedure

High-purity (99.9%) 12-μm W (Johnson Matthey, Ward Hill, MA), 99.5 percent-pure -325-mesh (equivalent to -44 μm) Ti (Micron Metals, Gates City, UT), and 99.9 percent-pure 2-μm graphite (CERAC Inc., Milwaukee, WI) were used in the majority of the experiments. Two other types of powders were also used: 99.95 percent-pure -325-mesh W and 99.0 percent-pure 10-μm Ti (Consolidated Astronautics, Inc., Milwaukee, WI).

The W and Ti powders were ball milled for several hours under an Ar atmosphere. In the precursor size matching experiments, the W:Ti ratio was fixed at 83:17 atomic-percent. Ratios of 100:0, 83:17, 70:30, 60:40, 51:49, and 0:100 atomic-percent were used in the dilution experiments. A Ti:C molar ratio of 1.0 was maintained in all of the Ti and C powder mixtures. The Ti and C powders were also dry mixed and ball milled under an Ar atmosphere. The Ti+C powder mixtures were uniaxially pressed at 44 MPa into 100-mm-outer-diameter, 50-mm-inner-diameter, and 20-mm-thick doughnut-shaped green compacts.

Shown in Figure 1(a), the CSA-HEC reaction vessel was designed to contain the Ti+C SHS reaction and serve as the die of a planar die-anvil explosive compaction fixture. The lid assembly of the reaction vessel functioned as the matching anvil. This anvil was fitted with a container that held the explosive charge. The fixture consisted of a mild-steel reaction vessel, W+Ti powder sample, doughnut-shaped Ti+C green compact, porous ZrO_2 (Zircar Products Inc., Florida, NY), graphite sheet insulation (Grafoil) (Grade GTA, Union Carbide, Cleveland, OH), Ti+B igniter mixture, electric igniter, and explosive driver package. The explosive driver package consisted of a set of high-hardness steel anvils, aluminum piston (lid assembly), poly vinyl chloride (PVC) container holding powdered Amatol (80:20 ammonium nitrate:TNT; detonation velocity, v_d = 3,850 m/s) explosive, C-4 Detasheet booster (DuPont Co., Wilmington, DE), and RP80 detonator (Reynolds Industries Systems, Inc., San Ramon, CA).

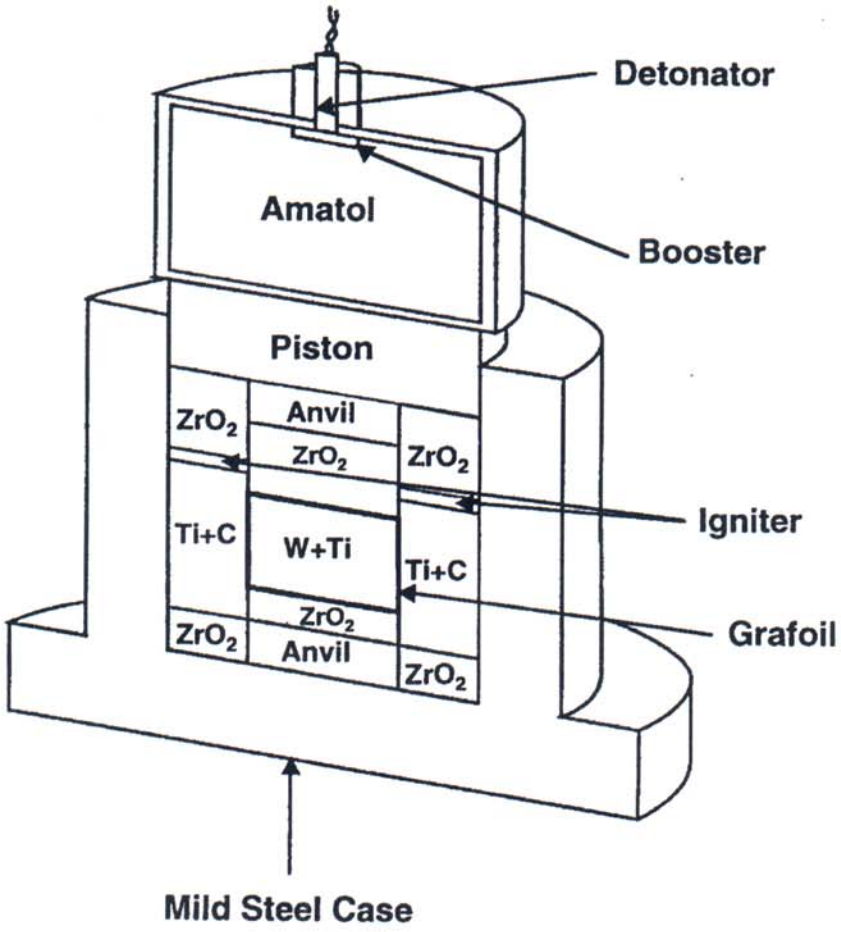

Figure 1(a). CSA-HEC method: (a) schematic diagram of the apparatus.

ZrO_2 insulation was required to reduce heat losses from the Ti+C reaction and to protect the piston-anvil assembly and explosives from overheating. Grafoil was to function as an inert barrier, preventing the diffusion of contaminants into the sample, and it also served to ease separation of the compacted components. Commercially available model-rocket igniters (Estes Industries, Penrose, CO) were used to initiate the SHS reaction.

The W+Ti powder sample was inserted into the Ti+C doughnut and surrounded with Grafoil and ZrO_2. The electric match and loose igniter powder were set atop the Ti+C green compact. The Al piston was partially inserted into the cavity, and the reaction vessel was sealed. The PVC container was loaded with the explosive. The container lid, with Detasheet attached to its underside, was fastened to the container, thereby completing the preparation sequence. The explosive-filled PVC container was then affixed to the top of the piston, and the completed assembly was placed on a sandpile.

Once the detonator was in place, the electric match was remotely activated, which , in turn, initiated the igniter mixture and Ti+C green compact. As the TiC reaction proceeded to completion, the enclosed W+Ti powder bed was heated (via diffusion) to high temperatures. The temperature profile of the W+Ti powder bed was measured in earlier experiments. Five equispaced thermocouples (TCs) were inserted into the W+Ti powder bed. TC1 and TC5 measured the edge temperature, while TC2, TC3, and TC4 were located in the interior. As shown in Figure 1(b), a unique feature of this preheating cycle is an isothermal condition that occurs approximately 60 s after the completion of the TiC reaction.

When the time to reach the isothermal plateau had elapsed, the piston-anvil, accelerated by the detonation of the explosive, densified both the sample and the TiC doughnut. The entire fixture was buried under sand, which served to protect the case and contents from excessive thermal shock. After the fixture and its contents returned to ambient temperature, the W-Ti billet was extracted.

The CSA-HEC experiments were conducted with optimized c/m (explosive charge mass to piston-anvil mass) and n_{TiC}/n_s (moles of TiC to moles of sample) [13]. The W:Ti ratio study was conducted with c/m of 1.85 ±0.12, while the n_{TiC}/n_s was held at 5.80 ±0.30. The lower c/m of 1.71, used for the pure metal billets, namely, W:Ti ratios of 100:0 and 0:100, was to minimize shock-induced damage. Experiments evaluating the effect of the size of the precursors were conducted with a c/m of 1.92 ±0.05 and n_{TiC}/n_s of 6.29 ±0.16. The consolidation of the Ti-coated W precursor powders was also performed near the optimum c/m, 1.87 ±0.26, but the n_{TiC}/n_s was higher, 7.30 ±0.21.

2.2 Sample Characterization

The postconsolidation evaluation of the samples consisted of macrophotography, bulk density determination, and analyses by SEM (JEOL, Inc., Peabody, MA), EDS (Noran Instruments, Middleton, WI), and XRD (Philips Electronic Instruments, Mahwah, NJ). The disk-shaped billets were cut into several roughly equal sections, and the mass density was measured with a water immersion technique.

The central region of the billets was further sectioned into thin wafers (parallel or perpendicular to the compaction direction) for SEM, EDS, and XRD analyses. The SEM samples were mounted and polished to a 1/4-μm finish. Much of the examination was performed with the SEM set in backscattered electron-compositional (BSE-COMPO) mode. The relative amounts of W and Ti in all of the samples were determined by a standardless semiquantitative analysis program, SSQ. The atomic percentages are based on the ratio of the Ti-Kα and W-Lα peak intensities. The precursor powder purities and

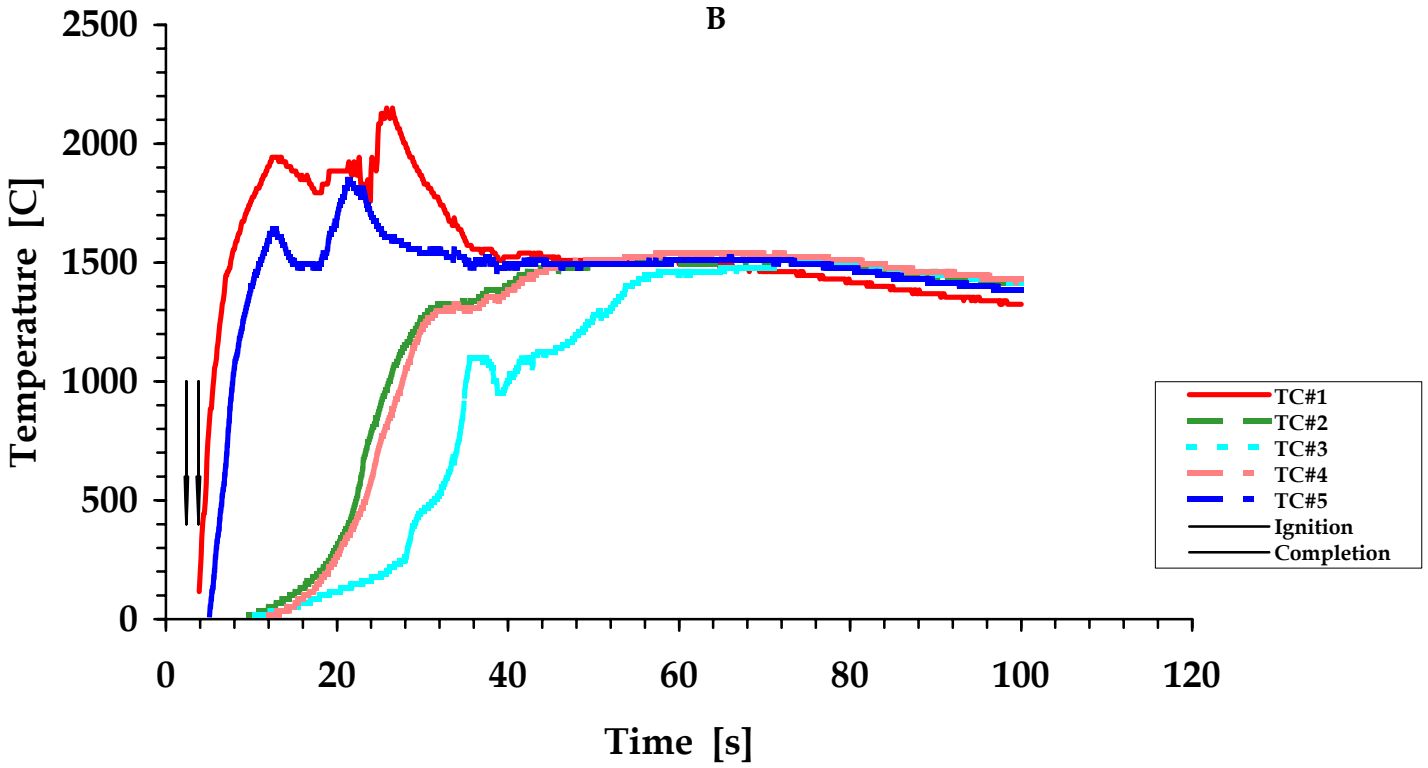

Figure 1(b). CSA-HEC method: (b) precompaction temperature history of the W+Ti powder bed.

morphologies (surface and cross-sectional) were also examined. The CSA-HEC wafer selected for the XRD analysis from the alloy billet was polished, sectioned to fit, and then mounted into a standard Al sample holder. Two sets of scans were obtained from each billet, one from the inner core and another from the periphery of the billet. Peripheral samples were usually fragmented pieces from the outer 5- to 6-mm edge region of the wafer because of the presence of laminar edge cracks in the billet. The precursor powders were subjected to XRD analysis as well, to obtain the "unstrained" (baseline) lattice parameter values. The samples were step-scanned through a 2Θ range of 20–120° using a 0.025° increment and a 5-s dwell time. The peak positions were based on a search of the minima of the second derivative of the scan. Lattice parameters were obtained using the intercept method [14].

Bulk microhardness measurements were performed using a Vickers indenter with 100- and 400-gf loads applied for 10 s. Listed values are averages from at least 20 individual hardness measurements. Quoted error bars represent the probable limit of error.

2.3 W Powder Coating Experiments

A physical vapor deposition (PVD)/DC sputtering system was modified to facilitate the production of Ti-coated W powder. As shown in Figure 2, an inclined, motor-driven servotray was located under a commercially pure (99.5 percent pure) Ti ion sputtering source. About 60 to 70 g of W was loaded, and, as the servotray rotated, the tilt caused the W particles to flow freely. The servotray was also periodically tapped by a spring-loaded hammer to facilitate the breakup of electrostatically charged agglomerates of W.

After the vacuum system was flushed with Ar several times, the sputterer power supply and associated cooling systems were turned on. The power level of the sputtering gun was approximately 200 W with an Ar background pressure of about 8.0×10^{-3} torr. With this relatively crude system, deposition rates of 0.05 to 0.06 g/hr were achieved.

The total mass gain (assumed to be attributable to Ti only) of each powder batch was measured and calibrated against the ratio of Ti-Kα and W-Lα EDS peaks. Typically, a CSA-HEC experiment necessitated the manufacture of four to five batches of coated W powder. The individual batches, made under the same conditions, were blended together into a single lot for each CSA-HEC experiment. Altogether, four lots of Ti-coated W were manufactured with 0.19 (0.05), 0.50 (0.13), 1.14 (0.30), and 2.67 (0.71) atomic-percent (weight-percent) of Ti.

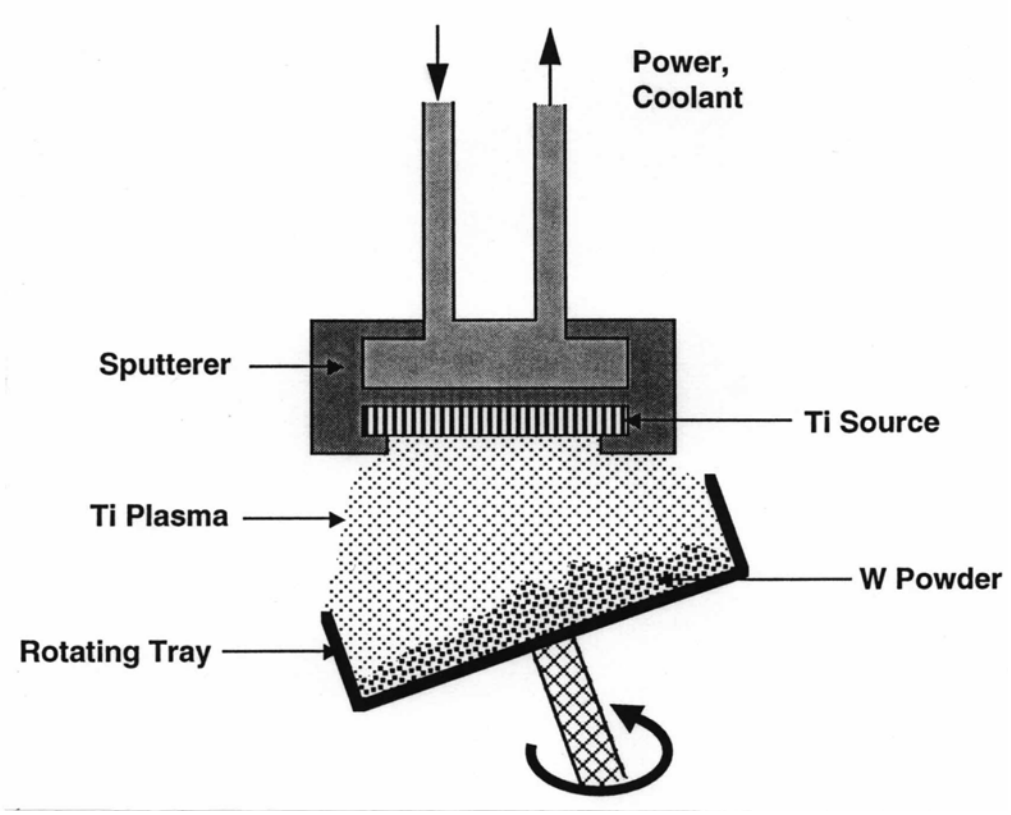

Figure 2. Schematic diagram of the PVD/DC sputtering system that was used to fabricate the Ti-coated W powder.

2.4 Post-Consolidation Annealing Treatments

Several wafers, cut from a 83W-17Ti billet, were vacuum annealed at 700, 1,000, or 1,400 °C. The level of vacuum was better than 1 H 10^{-5} torr. A heating rate of 5 °C/min was used to reach the soak temperature. The samples were soaked for 24 hr, slow cooled at 5 °C/min to 200 °C, and allowed to furnace cool to room temperature.

After the results of the initial annealing tests were assessed for modifications of the alloy microstructure, another 83W-17Ti billet was sectioned for additional heat treatments to be performed at 700 and 680 °C. The second set of annealing treatments was done at a different facility. The treatment at 700 °C was done to verify the consistency of the structural changes at the selected temperature, whereas two treatments at 680 °C were conducted to evaluate the effect of time at a fixed temperature. Thus, in the first two runs, the soak duration remained 24 hr; however, in the last run, it lasted 500 hr. The heating and cooling cycles at the second facility were run manually. At the onset of the temperature ramp, the maximum heating rate was approximately 23 °C /min, with an average heating rate of 15 °C /min. The soak temperature was reached in about 25 min. After the completion of the soak interval, the samples were allowed to furnace cool to

room temperature. The maximum cooling rate was about 10 °C /min, with an average cooling rate of 2.5 °C /min.

3. Results and Discussion

It has been shown that the n_{TiC}/n_s ratio significantly affects the heating rates and peak temperatures attained within the sample. More importantly, these measurements reveal that the time delay (60 s after the initiation of the TiC reaction) for the isothermal condition does not depend on the composition of the sample. For best results, the n_{TiC}/n_s ratio must be such that at the time of compaction the bulk of the sample will be approximately 1,550 °C, a temperature that is close to, but does not exceed the melting point of Ti (T_m = 1,670 °C), and excessive overheating of the periphery will be minimized. However, unless a large enough n_{TiC}/n_s ratio is used, the sample does not become isothermal at any point during the preheating cycle. The n_{TiC}/n_s ratio of about six satisfies both of these criteria. A more detailed description, mostly taken from Kecskes and Hall [13], is provided in the Appendix.

After compaction, the CSA-HEC samples had a diameter of 50 mm and an average thickness of 10 mm. The billets were compacted fairly uniformly with a density variation of about ±0.5%. The core was comprised of a disk with a diameter of about 35 to 40 mm, while the edge was comprised of the outer 10- to 15-mm annulus of the billet.

3.1 Size Control of the Matrix

Experiments with the 83W-17Ti composition were performed to reduce the preexisting size mismatch between precursors. It was presumed that under ball milling, the use of coarser W and/or finer Ti would disperse the W particle aggregates, thereby improving the uniformity within the billet. The precursors types, c/m, n_{TiC}/n_s, and percent TD values are summarized in Table 1.

Table 1. Precursor size effect on density.

Sample	W (μm)	Ti (μm)	c/m	n_{TiC}/n_s	Density (percent TD)
Standard	12	!44	1.98	6.23	98.9
Coarse	!44	!44	1.88	6.17	97.6
Fine	12	!10	1.91	6.47	99.4

Note: !44 μm is equivalent to !325 mesh.

Based on the billet densities, the use of coarse precursor particles hinders densification slightly; however, the use of fine Ti results in practically complete densification. A greater difficulty in the displacement of larger Ti particles is reflected in a reduced density. Improvement in rearrangement and movement of finer particles is indicated in a corresponding increase.

Shown in Figure 3, BSE-COMPO micrographs of core regions of the standard, coarse, and fine samples depict the resultant modification of the alloy substructure. In all of the samples, the edge-to-core structures are unaltered.

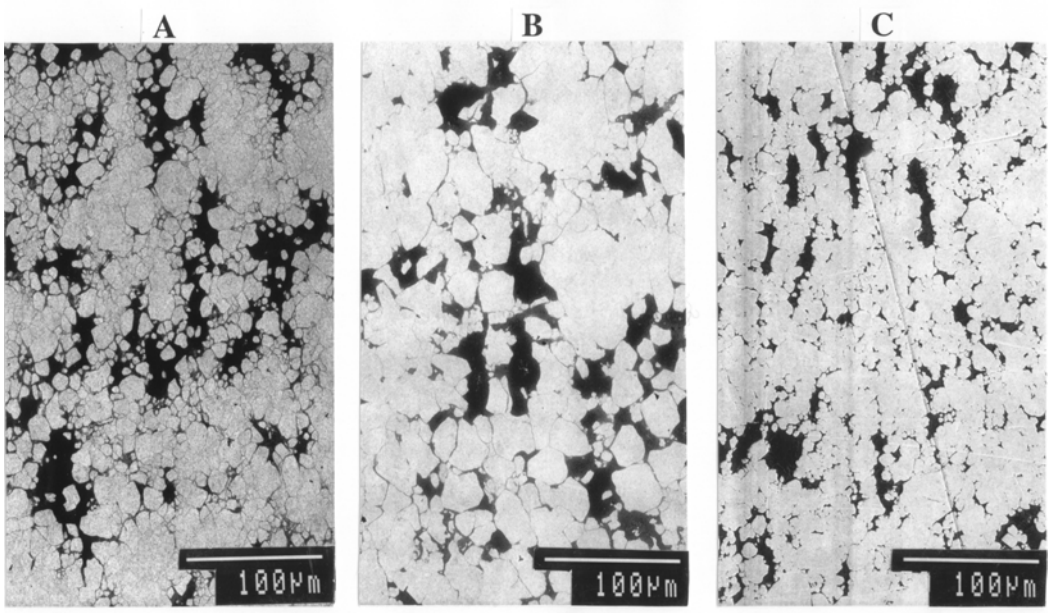

Figure 3. BSE-COMP micrographs of core regions of the 83W-17Ti alloys: (a) standard, (b) coarse, and (c) fine.

However, when the particle sizes are better matched, as is the case in the coarse sample, the dispersion of W grains appears to be most uniform, but at the expense of densification. Some improvement can also be observed in the fine sample. Overall, this sample seems to have a more elongated structure than the standard sample.

No significant modification of the alloy substructure (and only a relatively small improvement in the dispersion of the W grains) was observed with the variation of precursors. Therefore, beyond SEM examination of the grain morphology, no further analysis was performed on these samples.

3.2 Effect of the W:Ti Ratio on the Matrix

The alloys and unalloyed metals, with the corresponding c/m, n_{TiC}/n_s, percent TD, and microhardness values, are listed in Table 2. In previous density optimization experiments, a c/m of about 1.9 was found to produce samples with optimum (i.e., highest density without excessive cracking) results. To reduce sample damage, the pure samples were compacted with c/m below the optimum range. All of the alloy samples are near full density. The percent TD of the unalloyed metal samples are considerably lower than those of the alloy samples. A plausible explanation may be offered by considering the ratio of the temperature at compaction, T_c, to that of the melting point, T_m, T_c/T_m. Recall from Figure 1(b), T_c = 1,550 ^oC, and T_c/T_m is 0.45 for W and 0.93 for Ti. For W, the n_{TiC}/n_s is insufficient to elevate the powder temperature high enough to cause thermal softening. Consequently, during consolidation, the powder remains too stiff to be adequately densified. For Ti, the n_{TiC}/n_s is too high, rendering the outer periphery molten (or overly plastic), thereby sealing gas exit routes and preventing the complete elimination of the interior porosity.

Table 2. W:Ti ratio effects on density and microhardness.

Sample	c/m	n_{TiC}/n_s	Density		Microhardness (Gpa)	
atomic-percent			g/cm^3	percent TD	400 gf	100 gf
unalloyed metals						
W	1.72	6.12	19.35	96.6	3.8 ±0.1	4.1 ±0.1
Ti	1.70	5.60	4.507	95.6	1.9 ±0.1	2.0 ±0.1
alloys						
83W-17Ti	1.98	6.23	16.55	98.9	5.1 ±0.1	5.1 ±0.2
70W-30Ti	1.95	5.49	14.51	99.2	4.7 ±0.1	4.8 ±0.2
60W-40Ti	1.90	5.67	12.92	99.6	4.3 ±0.2	4.5 ±0.2
51W-49Ti	1.84	5.70	11.64	99.4	4.5 ±0.1	4.7 ±0.2

Representative longitudinal cross sections from the core regions of the sample billets are illustrated in Figure 4. The unalloyed and alloy samples are shown in Figure 4 (a–f). Discussion of the unalloyed metals is deferred for later.

The alloys contain structures consisting of W grain aggregates bounded by the Ti-rich β-Ti/W matrix. The W grains have retained their original size of 10–20 μm. In all cases, the dimension of the Ti-rich matrix generally corresponds to that of the Ti precursor. The matrix phase contains an equiaxed grain structure with a size of 5–10 μm. As evident in Figures 4(c–e), the effect of

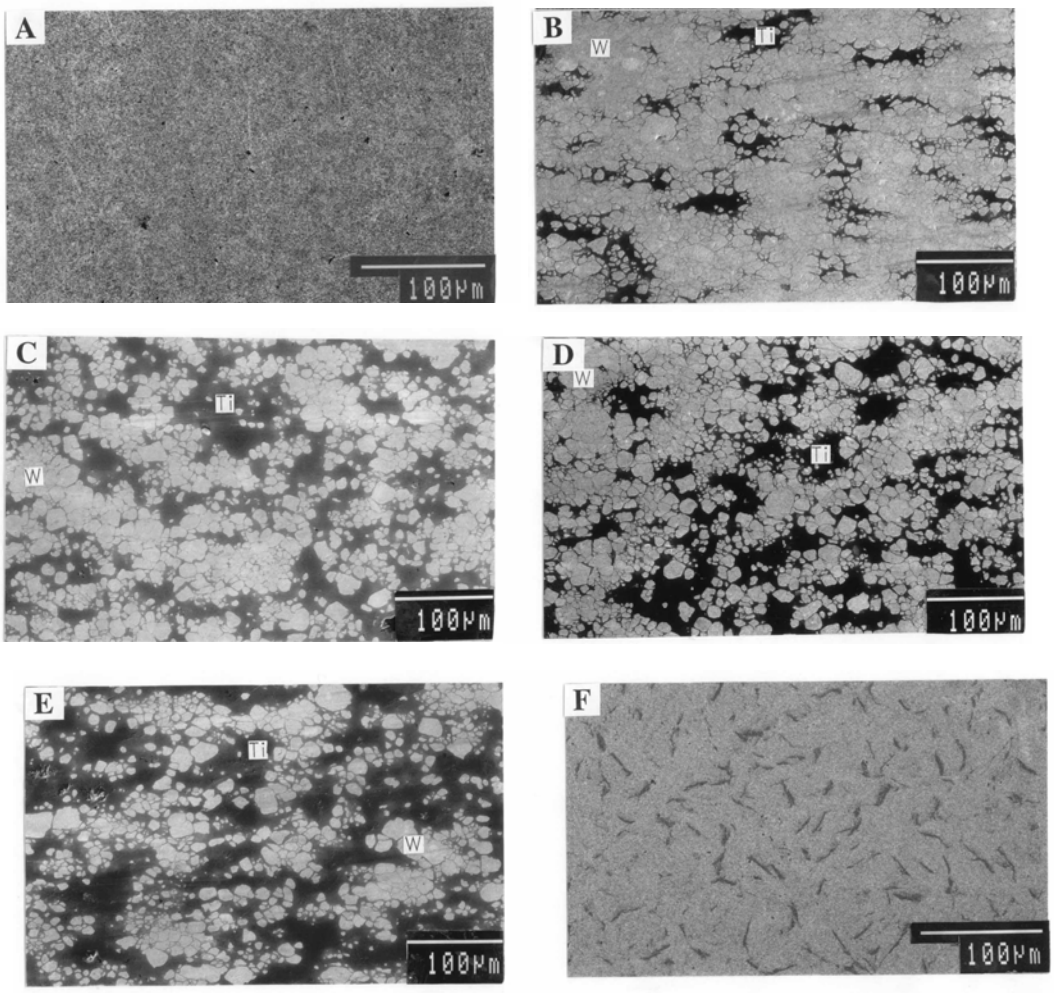

Figure 4. BSE-COMP micrographs of the alloys: (a) unalloyed W, (b) 83W-17Ti, (c) 70W-30Ti, (d) 60W-40Ti, (e) 51W-49Ti, and (f) unalloyed Ti.

dilution with increasing Ti content in the alloy is reflected in the breakup of the W agglomerates and the dispersion of the W grains. EDS of the samples indicated that in all cases, the W in the aggregates was nearly pure. In the 83W-17Ti sample, the Ti-rich phase had a composition of about 25W-75Ti. In the 70W-30Ti, 60W-40Ti, and 51W-49Ti samples, the amount of Ti in the matrix was higher, or about 15W-85Ti. Ti.

Shown in Figure 4(a), a BSE-COMPO micrograph of an etched cross section from the W sample core reveals an equiaxed grain structure. The preferential orientation seen in the alloys is absent. The precursor W powder morphology is retained, with some fine porosity remaining along grain boundaries. As is apparent from SEM, taking note of the extremely high Tm W, it may be concluded that the n_{TiC}/n_s used generates insufficiently high temperatures in the interior of the W powder bed to optimize compaction.

In Figure 4(f), a BSE-COMPO micrograph of an etched cross section of the Ti sample core region shows randomly distributed, heavily deformed grains with a secondary, darker phase between grains. From the appearance of the grains, it may be concluded that in the interior the temperature does not exceed $T_m T_i$.

The grain-boundary phase can most likely be attributed to the TiO_2 surface film stripped away during consolidation. Figures 5 and 6 show the core and edge XRD scans for the six alloys. Because the core and edge results differed, the cores are discussed first.

XRD of the sample cores verified that the primary phase consists of W only and that the secondary, matrix phase is a Ti-rich β-Ti/W solid solution. Typically, the XRD scans consist of peaks from the W grains, the β-Ti/W solid solution, and the Al sample holder. The signal level from the holder is below 0.5%. As seen in Figure 5, the diffraction peaks corresponding to W can be clearly recognized. In the core of the unalloyed W sample (Figure 5[a]), the scan reveals only W peaks. With an average lattice parameter of 0.31636 ±0.00004 nm, the W peaks are slightly shifted. The W powder yielded a baseline value for the lattice parameter of 0.31599 ±0.00007 nm (the nominal lattice parameter of W is 0.31652 nm) [15].

The core scans from the alloys are displayed in Figure 5 (b–e). In the alloy cores, the W peaks shift the same amount (when compared to the precursor W), with an average lattice parameter of 0.31635 ±0.00004 nm. With increasing Ti in the samples, most of the β-Ti/W diffraction peaks become visible. The secondary peaks correspond to a body-centered-cubic (bcc) structure with an average lattice parameter of 0.3254 ±0.0002 nm. This lattice parameter corresponds [16] to a β-Ti/W solid solution with a composition of 11W-89Ti ±1. Aside from a shoulder on the (110) W peak, the XRD scan (Figure 5[b]) of the 83W-17Ti sample does not reveal any of the higher angle β-Ti/W peaks.

An XRD analysis of the pure Ti billet core (Figure 5[f]) indicated that the sample is α-Ti only. In the absence of W, a β-Ti stabilizer, this result is expected. The lattice parameters of the core region of the pure Ti sample and the Ti precursor powder are slightly different. The Ti sample yields the values of 0.29502 ±0.00007 nm for a_0 and 0.46487 ±0.00002 nm for c_0, and a c_0/a_0 of 1.5757 ±0.00037. A scan of the Ti powder yields 0.29440 ±0.00018 nm for a_0 and 0.46680 ±0.00320 nm for c_0, with a c_0/a_0 of 1.5856 ±0.0109. (The nominal values for Ti are a_0 = 0.29503 nm, c_0 = 0.46831 nm, and a c_0/a_0 of 1.5873.) Notice the slight lattice distortion in the Ti sample.

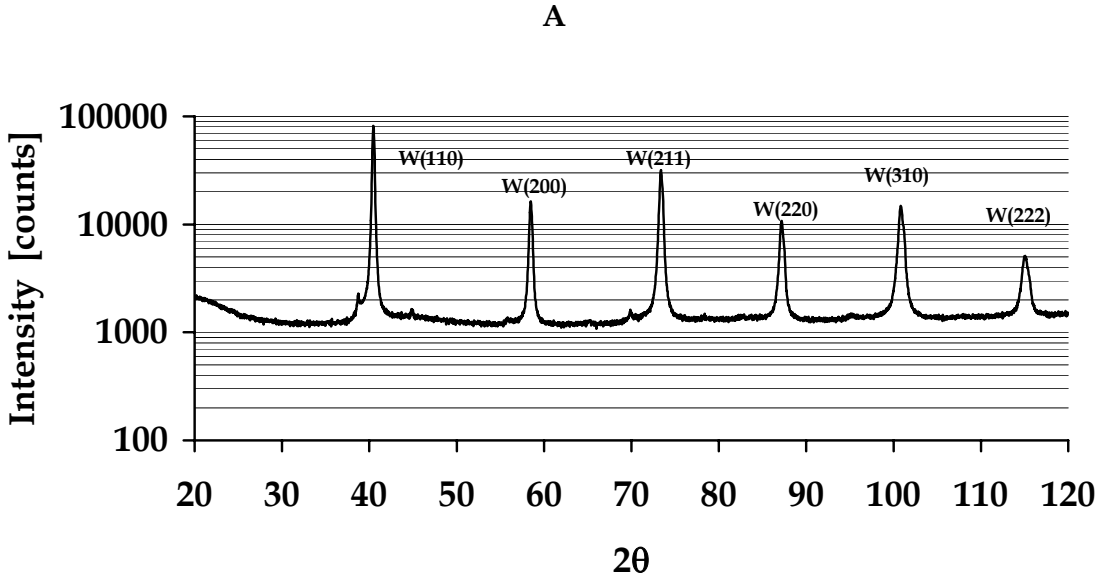

(a) Unalloyed W

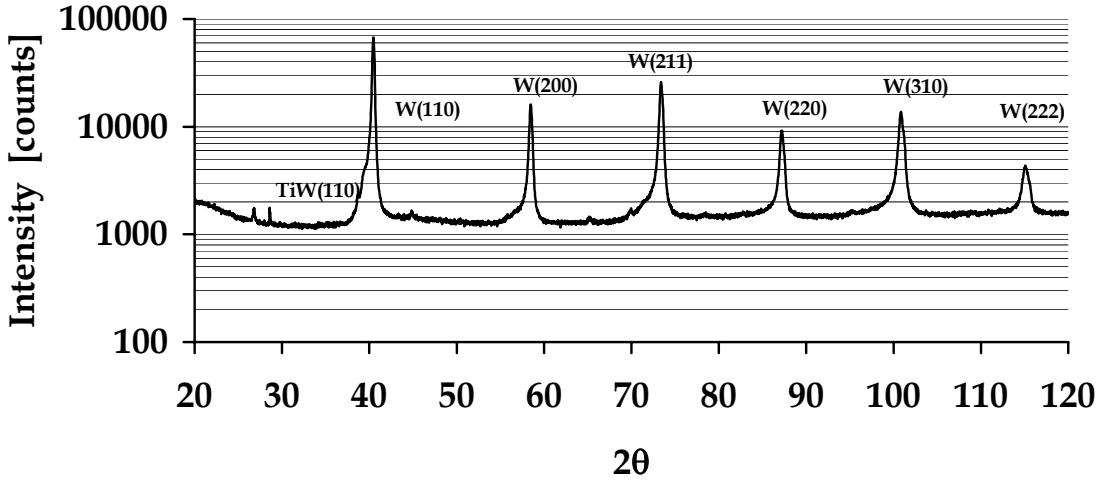

(b) 83W-17Ti

Figure 5. XRD scans of the CSA-HEC sample cores: (a) unalloyed W, (b) 83W–17Ti, (c) 70W–30Ti, (d) 60W–40Ti, (e) 51W–49Ti, and (f) unalloyed Ti.

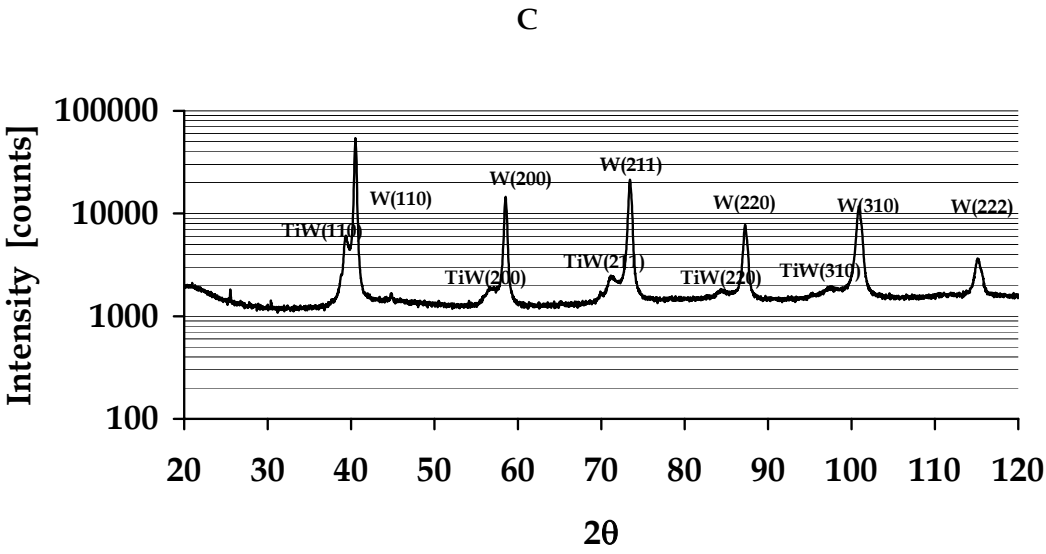

(c) 70W-30Ti

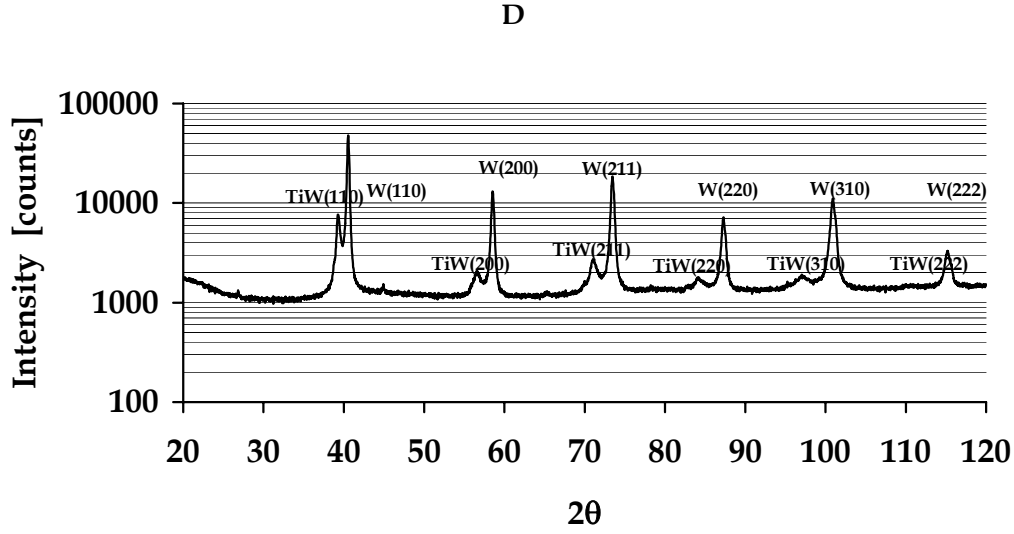

(d) 60W-40Ti

Figure 5. XRD scans of the CSA-HEC sample cores: (a) unalloyed W, (b) 83W–17Ti, (c) 70W–30Ti, (d) 60W–40Ti, (e) 51W–49Ti, and (f) unalloyed Ti (continued).

E

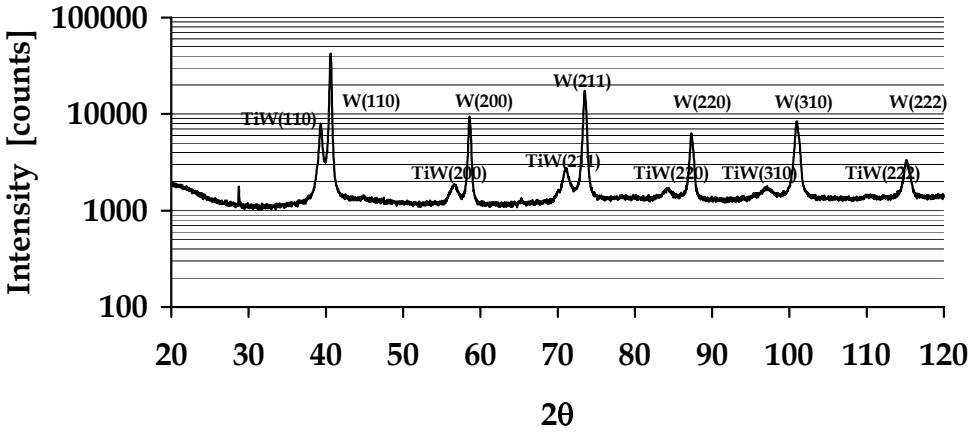

(e) 51W-49Ti

F

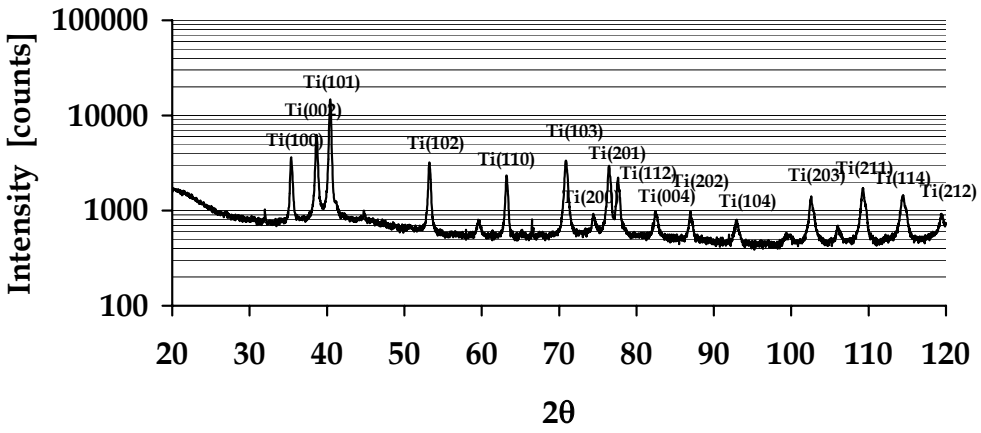

(f) Unalloyed Ti

Figure 5. XRD scans of the CSA-HEC sample cores: (a) unalloyed W, (b) 83W–17Ti, (c) 70W–30Ti, (d) 60W–40Ti, (e) 51W–49Ti, and (f) unalloyed Ti (continued).

A

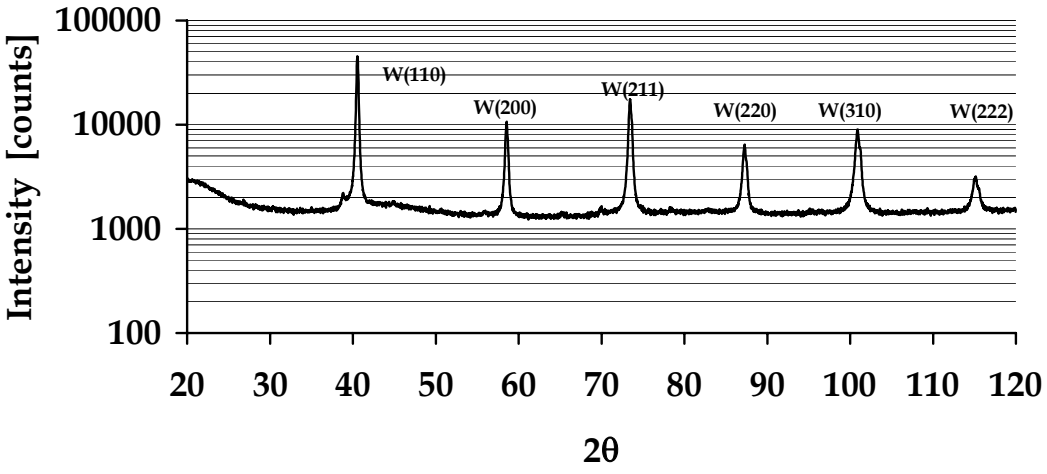

(a) unalloyed W

B

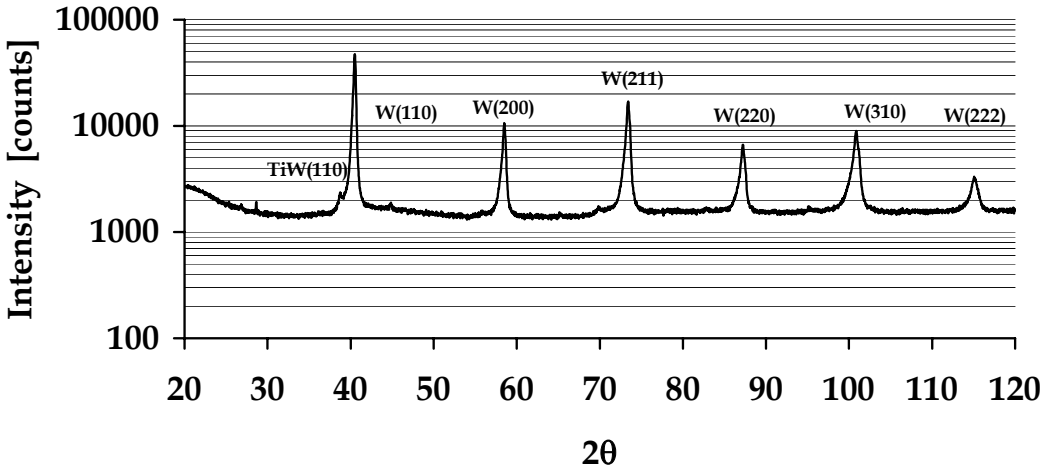

(b) 83W-17Ti

Figure 6. XRD scans of the CSA-HEC sample edges: (a) unalloyed W, (b) 83W–17Ti, (c) 70W–30Ti, (d) 60W–40Ti, (e) 51W–49Ti, and (f) unalloyed Ti.

C

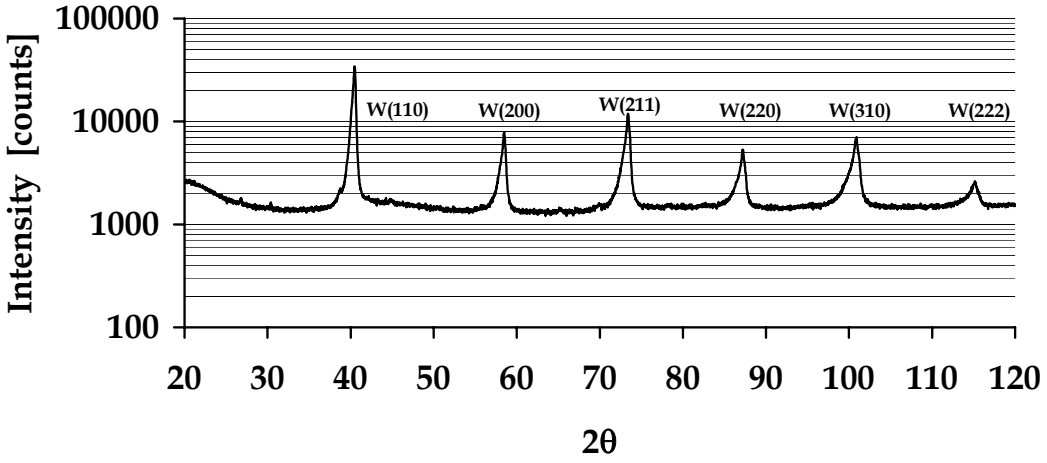

(c) 70W-30Ti

D

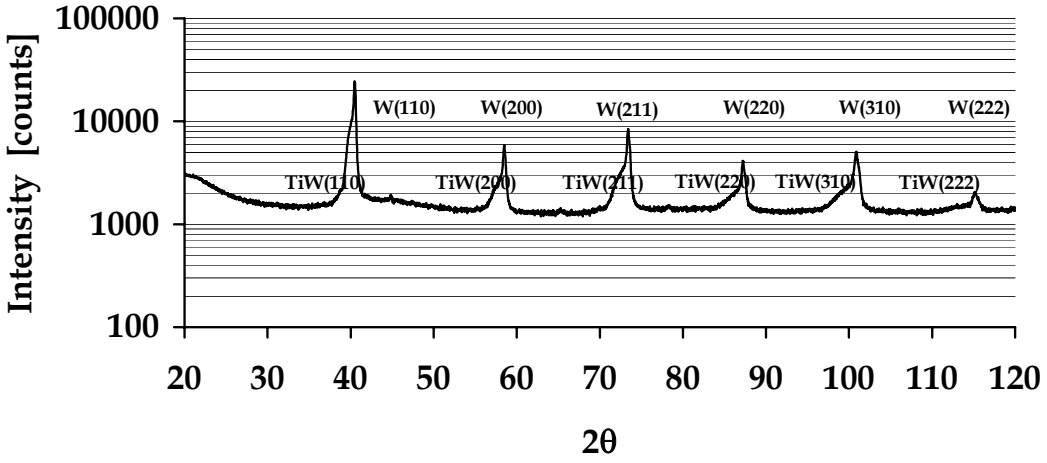

(d) 60W-40Ti

Figure 6. XRD scans of the CSA-HEC sample edges: (a) unalloyed W, (b) 83W–17Ti, (c) 70W–30Ti, (d) 60W–40Ti, (e) 51W–49Ti, and (f) unalloyed Ti (continued).

E

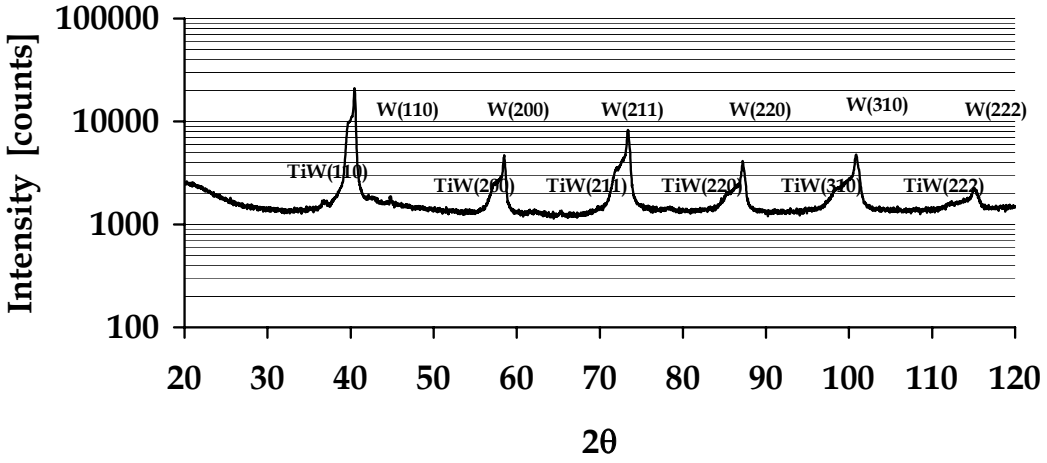

(e) 51W-49Ti

F

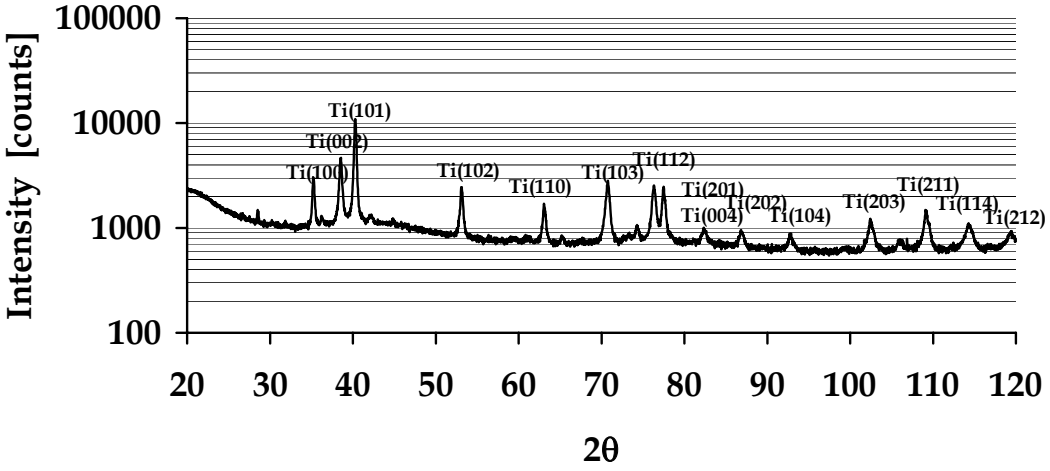

(f) unalloyed Ti

Figure 6. XRD scans of the CSA-HEC sample edges: (a) unalloyed W, (b) 83W–17Ti, (c) 70W–30Ti, (d) 60W–40Ti, (e) 51W–49Ti, and (f) unalloyed Ti (continued).

The microstructures of the edge and transition regions of the more diluted alloy samples reveal only minor deviations from that of the 83W-17Ti sample. Core regions are somewhat wider, however, at the expense of a narrower, or more compressed, transition region. The edge regions appear to be generally unaffected. The higher Ti content within these regions predominantly produces a wider, but not a more dilute, Ti-rich β-Ti/W matrix. An EDS analysis of these regions was consistent with earlier results.

XRD scans collected from the edge regions of the billets are shown in Figure 6. The scan of the pure W sample (Figure 6[a]) contains peaks due to W only. The lattice parameter, 0.31610 ±0.00004 nm, obtained for W in the sample, reflects a slightly more stressed crystal lattice than in the core region of the sample. The scan from the edge of the pure Ti sample is shown in Figure 6(f). As before, the scan corresponds to α-Ti. The values of 0.29509 ±0.00007 nm for a_0 and 0.46591 ±0.00003 nm for c_0 correspond to a c_0/a_0 of 1.5789 ±0.00037.

The alloy edge scans are displayed in Figure 6(b–e). The W peaks yield an average lattice parameter of 0.31632 ±0.00013 nm, which is essentially the same as that of the core. An immediate difference of the edge scans from those of the cores is the absence of the well-defined series of peaks attributed to the Ti-rich β-Ti/W matrix. Instead of a "fixed" composition as observed before, a gradual decay of the low-angle leading edge of the W peaks is present. This represents a range of β-Ti/W solid solution compositions (i.e., the sum of a series of smaller peaks).

When compared to the precursor W, the lattice parameter values of W in the unalloyed metal and alloy cores reflect that the deformation (if any) induced by the CSA-HEC process is also removed during the process. Scanning electron microscopy (SEM) of the edge regions of the metal and alloy billets shows more shear-deformed W grains. However, due to the proximity of the hot TiC and the resulting thermal softening, the distortion of the lattice parameter is negligible.

The difference in XRD results between the edge and core scans can be interpreted by referring to the precompaction thermal history of the W-Ti sponge [13] and the diffusivity of W in α- and β-Ti (see Figure 1[b]). In the core, the temperature rises gradually to 1,550 °C, the isothermal plateau. Because of the moderately high diffusivity of W in Ti [17] and the fact that all of the samples are consolidated at the same delay time (i.e., at the same temperature during preheating), it is expected that the β-Ti/W solid solution in all of the alloys would equilibrate at one composition. In other words, in all instances, during the precompaction period, only a fixed amount of W may dissolve into Ti. Subsequent movement of W within Ti is by rapid diffusion, rendering a single, essentially uniform composition to the matrix. In the absence of a composition gradient that would be introduced by slow diffusion, the rate-controlling step of the CSA-HEC process is the (solid-state) dissolution of W into Ti. EDS

measurements, reflecting only a 5% compositional increase from edge to center within the matrix, are consistent with this hypothesis.

The edge of the billet undergoes an entirely different thermal cycle. Specifically, it is heated to higher temperatures of about 2,000 °C, above the solidus, into the two-phase region that accelerates the dissolution process (see Figure 7 for the W-Ti phase diagram). This accounts for a higher W content in the β-Ti/W solid solution. Again, fast diffusion equilibrates the composition. However, the existence of a thermal gradient at the edge, ~60 °C /mm, renders the peak temperature to be spatially dependent and causes nonuniform dissolution of W. That is, the extent of W dissolution is determined by the given temperature at a given location within the edge region of the billet.

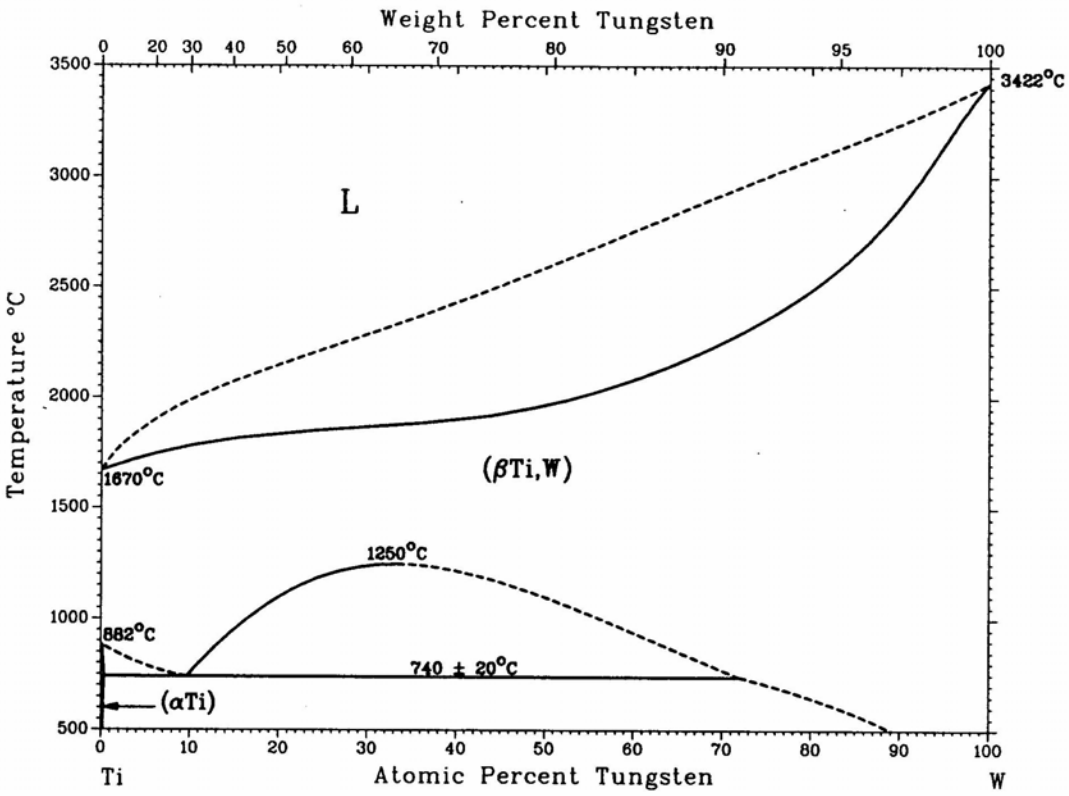

Figure 7. W-Ti equilibrium phase diagram.

When compared to the other alloys, the somewhat lower Ti level in the matrix of the 83W-17Ti alloy can be explained by considering the sample's morphology (recall Figure 4) in conjunction with the high diffusivity of W in Ti. In the 83W-17Ti alloy, the average width of the Ti-rich regions, or interparticle distance between W grains, is considerably less. When compared to the other alloys, there are fewer Ti particles in the 83W-17Ti alloy that are surrounded by a larger number of nearest neighbor W grains. Thus, when the Ti moves to wet the

adjacent W grains, the available amount of Ti for each W grain is less. Consequently, the solid solution layer will be thinner. Then, during the precompaction heating phase, more W can diffuse into the thinner Ti layer, thereby rendering it more W rich.

As evident in Table 2, microhardness measurements of the W-Ti alloy samples reflect a significant increase in overall hardness when Ti is added to W. This increase is caused by the formation of the Ti-rich β-Ti/W solid solution. But with an increasing solid solution content in the alloy, the effect of hardening diminishes. In addition to the effect of dispersion, the CSA-HEC samples also exhibit the effect of shock hardening. Though not tabulated, the hardness of the uncompacted W and Ti precursor powders was measured as well. While the hardness of the CSA-HEC W sample was about 10% higher than that of the W powder, the hardness of the CSA-HEC Ti was approximately four times larger than that of the Ti powder. Thus, while the effect of dispersion (i.e., solid-solution hardening) is more significant at small Ti additions, the effect of shock consolidation is more significant on the Ti component.

3.3 Coated W Powder Effects of the Matrix

Although dilution eliminated the contiguity of the W grains, the resultant alloys had considerably lower densities than desired. Consequently, an alternate method was undertaken to disperse the W grains within the alloy. It was surmised that a thin Ti coating layer on the W grains would not only eliminate the problems associated with the W-W contiguity, but also retain the required high density. A similar concept was used by Ultramet Corp. to utilize a modified fluidized-bed chemical vapor deposition method to coat W with Ni/Fe [18] or Hf [19], and then densify the coated powder with a Ceracon forging (essentially a hot-isostatic) process [20].

A PVD/DC sputtering process was chosen to coat the W powder [21]. In spite of general difficulties associated with coating W [22] and inherent differences between W and Ti (i.e., different T_ms, densities, and coefficients of thermal expansion), the method was successful in producing a thin yet continuous coating on W particle surfaces.

The results of initial experiments varying the coating time, sputtering power, and Ar pressure were as expected. The mass gain was directly proportional to the duration of the coating time. As the amount of Ti increased on the powder surface, electrostatic attraction between particles became more pronounced. Due to extensive agglomeration, the overturning flow of the powder diminished after several hours (four or more). The quasi-stationary powder mass, formed into clumps, was separated by gaps that allowed only limited sliding in the tray. Upon allowing the agglomerated mass to cool by shutting off the sputterer and venting the chamber with Ar to ambient pressure, the clumps disappeared and

the powder was again able to flow without any difficulty. This iterative technique was used to attain mass gains above 1.89 atomic-percent (0.50 weight-percent).

An increase or decrease in the sputter power level altered the deposition rate. A 50% power level decrease resulted in a noticeable drop in mass gain. A 50% increase in power level caused more rapid heating and agglomeration of the powder, but without a significant mass gain. The deposition rate was found to be insensitive to a change in Ar pressure. The mass gain remained unchanged with a two-fold increase of the Ar pressure, but dropped considerably with a four-fold increase.

In the final coating runs of W with Ti, four grades of coated powders were fabricated with 0.19 (estimated from EDS-mass gain calibration), 0.50, 1.14, and 2.67 atomic-percent of Ti on W. SEM indicated that the Ti layer was generally nonuniform, due to agglomeration and poor flow. However, the combination of automatic deagglomeration at removal of the powder from the vacuum chamber, the blending of the different batches, and the movement of particles upon consolidation reduced the significance of this effect.

Figure 8 depicts BSE-COMPO micrographs of the core regions of the CSA-HEC samples fabricated from the four different grades of coated powder. In the figure, note the development of a uniform boundary layer. EDS was used to verify that this layer contained Ti, but even a spot analysis could not definitively determine the W:Ti ratio in the narrow intergrain boundary layer. Figures 8(a and b) show that at the 0.19- and 0.50-atomic-percent levels, the Ti resides within grain triple junctions only. At 1.14 atomic-percent of Ti (Figure 8[c]), the boundary layer is continuous, but remains localized and irregular. However, in Figure 8(d), at 2.67 atomic-percent of Ti, the W-W grain contiguity is virtually eliminated.

More detailed examination of the sample billets revealed that the usual edge-to-core structure of the 83W-17Ti alloy was inapplicable to these samples. Instead, their morphologies more closely resembled the structure of the unalloyed W billet.

3.4 Post-Consolidation Anneal Control of the Matrix

Examination of the annealed samples indicated that increasing temperatures significantly alter the 83W-17Ti alloy microstructure. The heat treatments of 24 hr at 680, 700, 1,000, or 1,400 °C, as well as the longer 500-hr treatment at 680 °C, resulted in the modification of the Ti-rich matrix. The selected temperatures were insufficient to cause rearrangement and, therefore, did not increase the dispersion of the W grains.

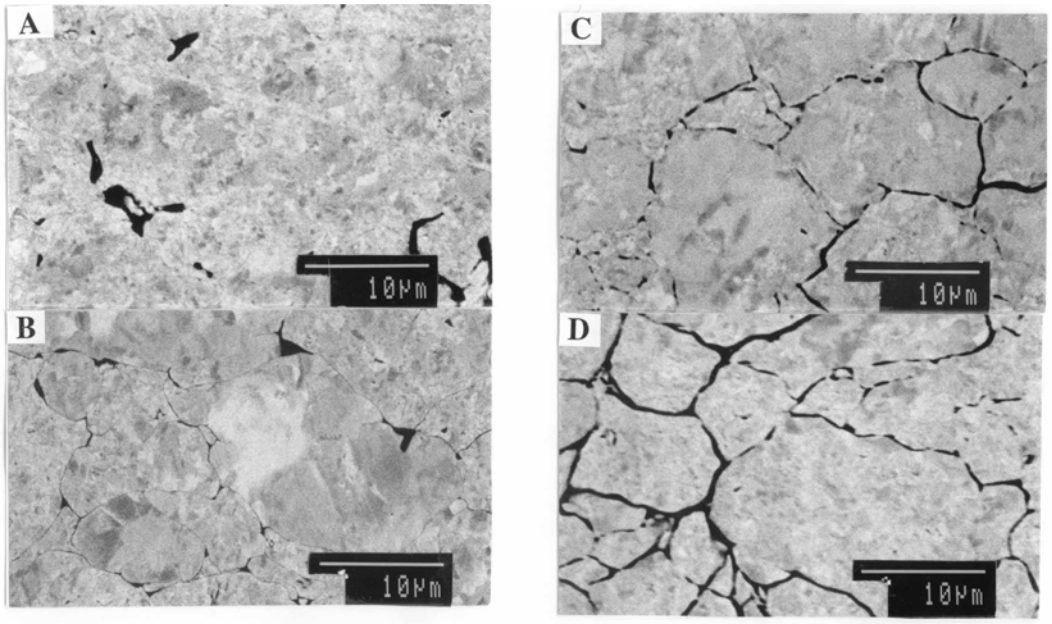

Figure 8. BSE-COMP micrographs of the core regions of W-Ti alloys fabricated from Ti-coated W powder: (a) 0.19 Ti atomic-percent, (b) 0.50 Ti atomic-percent, (c) 1.14 Ti atomic-percent, and (d) 2.67 atomic-percent Ti.

The types of microstructures formed in the annealed samples were in general agreement with the equilibrium W-Ti phase diagram (see Figure 7). As illustrated in Figures 9 (a and b), at 700 and 1,000 °C, the notable features are similar to those found in the various regions of the untreated 83W-17Ti sample (see Figure 5[b]). Although the appearance of the Ti-rich matrix is altered, the W grain morphology is preserved and the overall regional edge-to-core delineation is retained as well. At 700 °C, the initially homogeneous Ti-rich matrix at the sample core region decomposes into monotectoid structures only. At 1,000 °C, intergrain and intragrain precipitates from within the Ti-rich matrix. At 1,400 °C (Figure 9[c]), the original alloy structure is lost and replaced entirely by a uniform structure of W grains surrounded by a W-rich solid solution.

The second series of 24-hr anneals at 680 or 700 °C primarily brought about the formation of submicrometer-sized Ti-rich spheroids at grain boundaries within the matrix. The degree of coarsening was somewhat more noticeable at the higher temperature. Neither anneal had an impact on the overall substructure of the matrix. Associated with the appearance of the spheroids, minor monotectoid decomposition was also observed during the second series of anneals. The varying extent of monotectoid decomposition in the two 700 °C anneals was within the approximate ±10 °C maximum limit of error in oven temperatures.

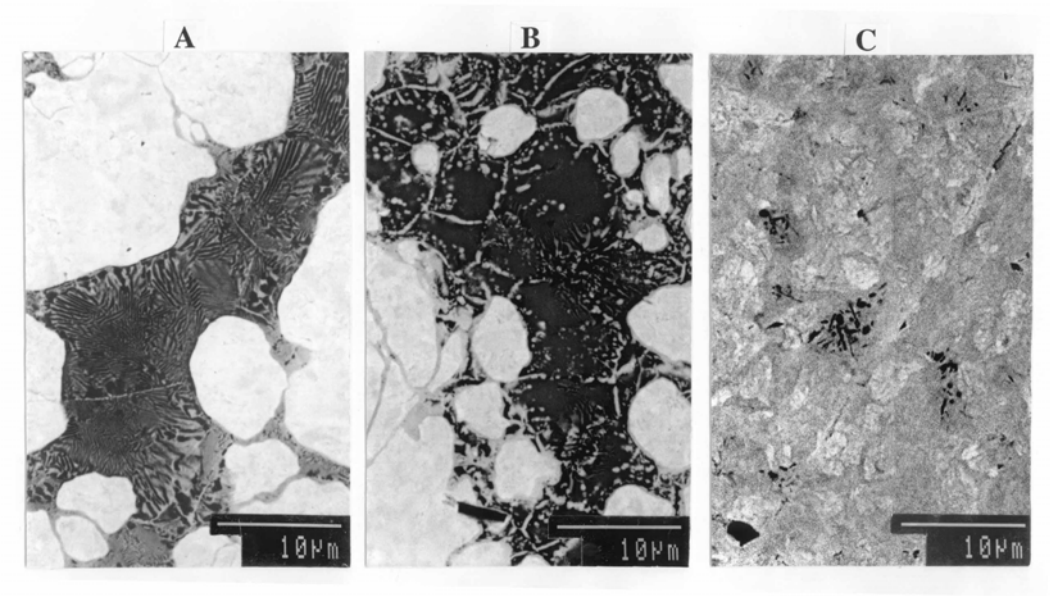

Figure 9. BSE-COMP micrographs of substructures forming during annealing: (a) 700 °C, (b) 1,000 °C, and (c) 1,400 °C.

The anneals at 700 °C uncovered an important deviation from the phase diagram. Monotectoid decomposition was found to occur at a lower temperature than predicted. Since even a maximum deviation of 20 °C error in oven temperatures cannot easily account for this discrepancy, the role of impurities and contaminants must be considered.

The manufacturer's spectrochemical analysis of the W and Ti powders indicated the metallic impurities of Cr, Fe, Ni, and Na with a combined level of less than 0.01 atomic-percent (100 ppm). During preparation and processing, the W and Ti powders could only be exposed to air and water vapor. It is estimated that the level of these contaminants is at most an order of magnitude higher, or 0.1 atomic-percent (1,000 ppm). Physisorbed water vapor decomposes on the powder surface to form hydrides and oxides. Hydrogen has an extremely low solubility in W and a slightly higher solubility in Ti at room temperature. Therefore, any hydrogen adsorbed from moisture at higher temperatures will not be retained upon cooling. In contrast, the oxides of both W and Ti are relatively stable with respect to decomposition at high temperatures [23].

In the CSA-HEC fixture, the W+Ti powder bed, though protected by the reducing environments of the TiC chemical furnace and the Grafoil sheet, may still be exposed to oxygen and nitrogen from air. Except for carbon from the Grafoil, no other elements from the surrounding environment come into contact with the W+Ti powder bed during fabrication. The metal impurities are β-Ti stabilizers, whereas carbon, nitrogen, and oxygen interstitials are all α-Ti stabilizers [23, 24]. A simple calculation [25] of the depression/elevation of the transition point reflects a net effect that would tend to elevate the equilibrium monotectoid temperature by about 5 °C. Therefore, based on the expected

behavior of the impurities, the experimental observations, and lack of other explanations, it may be concluded that the monotectoid reaction, βTi/W > α-Ti + W, must occur at a temperature of 700 ±10 °C. This result is close to the 715 °C given by Maykuth's assessment [26], but differs from Murray's calculation [27] of the current W-Ti phase diagram that places the monotectoid at 740 ±20 °C.

Further discrepancies with the W-Ti phase diagram have also emerged. Lo [28] has reported that the miscibility gap maximum ought to be higher, at 1,350–1,400 °C. Murray [27] claimed that a shift of the monotectoid to a lower temperature disallows the proper position of the β/(α+β) phase boundary. Since that calculation was based on a maximum of 1,250 °C, a higher miscibility gap maximum may yield results more consistent with the lower monotectoid temperature.

The anneal at 1,000 °C resulted in structural changes (inter- and intragrain precipitation) consistent with the expected phase separation within the gap. At 1,400 °C, an essentially uniform, single-phase matrix was observed. Although the matrix composition moved beyond the miscibility gap, its uniformity indicates that no phase separation occurred at this temperature. This is in agreement with Lo's placement [28] of the critical point temperature at about 1,350 °C. Unfortunately, due to the limited extent of this effort, the critical point composition was not assessed. Nevertheless, in light of this work and Lo's previous disagreement [28] with the miscibility gap maximum, the W-Ti phase diagram should be reassessed.

After 500 hr at 680 °C, the types of changes in the matrix were similar to those already noted for the 24-hr treatments at 680 and 700 °C. The advanced coarsening process was evident in the widening and spheroidization of monotectoid structures, enlargement of existing Ti-rich spheroids (especially near subgrain boundaries within the matrix), and further phase separation at intergrain regions.

The size of the Ti-rich spheroids in the sample treated for 500 hr at 680 °C reflects the sluggish dissociation of the initially homogeneous matrix. Given an annealing time of 1.8×10^6 s and a small spheroid size of about 1–2 μm, the phase separation that resulted from this treatment indicates that postconsolidation control of the matrix structure is impractical. Extensive dissociation of the β-Ti/W solid solution, even at the maximum allowable temperature just below the monotectoid temperature, is expected to be nearly impossible. Even at the maximum allowable temperature (i.e., below the monotectoid temperature), extensive dissociation of the β-Ti/W solid solution was not observed.

Although annealing was expected to promote intergranular bonding, microhardness measurements from the annealed samples do not reflect a substantial improvement. The microhardnesses of the untreated and treated 83W-17Ti alloys are listed in Table 3.

Table 3. Annealing temperature effect on microhardness; 83W-17Ti.

Sample	Density (percent TD)	Annealing Temperature (°C)	Microhardness (GPa)	
			400 gf	100 gf
1118	98.3	—	5.0 ±0.1	5.0 ±0.1
1118	98.3	700	n/m[a]	5.2 ±0.2
1118	98.3	1,000	n/m[a]	5.3 ±0.1
1118	98.3	1,400	n/m[a]	4.7 ±0.2
1123	98.9	—	4.8 ±0.1	5.2 ±0.2
1123	98.9	680	4.8 ±0.0	5.0 ±0.1
1123[b]	98.9	680	4.9 ±0.1	5.2 ±0.1
1123	98.9	700	5.1 ±0.0	5.3 ±0.1

[a] Not measured.
[b] Sample annealed for 500 hr.

The 100- and 400-gf microhardnesses of the untreated alloys are about 4.9 ±0.1 GPa and 5.1 ±0.1 GPa, respectively. The introduction of monotectoid structures at 700 °C and fine precipitates at 1,000 °C does not cause the microhardnesses of the alloy to shift. At 1,400 °C, there is a modest reduction in microhardness to 4.7 ±0.2 GPa, which corresponds to the modification of the sample microstructure. The microhardness values of the second anneal series of samples are consistent with those of the first series. The effect of the higher sample density is negligible. The longer duration annealing does not change the microhardness of the alloy.

4. Conclusions

Full-density W-Ti alloy billets were fabricated with a CSA-HEC technique. The W+Ti powder bed was preheated via conduction by the heat release of a Ti+C combustion synthesis reaction, and when the bed was isothermal, it was consolidated by the detonation of an explosive. The W-Ti alloys were compacted with good results because the softer Ti-rich matrix deformed easily, filling voids between the harder W aggregates. In contrast, neither of the two pure metals compacted well. At the compaction temperature, Ti was too plastic, whereas W was too stiff. The presence of one of the metals in the absence of its complement, the stiffer or softer phase, degraded the compactibility of the powder bed.

The inner core of the billet formed by this method consisted of W particle agglomerates surrounded by a partially continuous Ti-rich β-Ti/W matrix. Lattice parameter data and hardness measurements indicated that the alloys are affected by solution hardening. The experiments have addressed one of the three major characteristics imposed by the CSA-HEC process on the W-Ti alloy billet,

the incomplete dispersion of the Ti phase. Improvement in matrix phase dispersion with the use of finer Ti or coarser W was limited. Dispersion was most enhanced by dilution, but yielded billets with significantly lower densities. A PVD method was developed for the coating of W with Ti to create a uniform dispersion of Ti in the W-Ti alloy. The overall dispersion was improved without a loss in sample density.

Post-consolidation annealing did not result in a rearrangement of the billet's spatially dependent structure. Heat treatments altered the characteristics of the matrix only. More importantly, however, the annealing treatments uncovered inconsistencies in the current W-Ti phase diagram. Monotectoid decomposition occurred at a temperature of 700 ±10 °C, which was lower than expected. An upper temperature bound of 1,400 °C for the critical point was also established, consistent with another recent assessment of the W-Ti system.

5. References

1. Meyers, M. A., and L. E. Murr (editors). *Shock Waves and High-Strain-Rate Phenomena in Metals: Concepts and Applications*. New York: Plenum Press, 1981.
2. Murr, L. E., K. P. Staudhammer, and M. A. Meyers (editors). *Metallurgical Applications of Shock Wave and High Strain Rate Phenomena*. New York: Marcel Dekker, 1986.
3. Cross, A. *Iron Age*. Vol. 184, pp. 48–50, 1959.
4. Gorobtsov, G., and O. V. Roman. *Int. J. Powder Metall*. Vol. 11, pp. 55–60, 1975.
5. Bhalla, A. K. *Trans. Powder Metall. Assoc. Ind*. Vol. 7, pp. 1–8, 1980.
6. Wang, S. L., M. A. Meyers, and A. Szeket. *J. Mater. Sci*. Vol. 23, pp. 1786–1804, 1988.
7. Ferreira, A., M. A. Meyers, N. N. Thadhani, S. N. Chang, and J. R. Kough. *Metall Trans. A*. Vol. 22A, pp. 685–695, 1991.
8. Shang, S. S., K. Hokamoto, and M. A. Meyers. *J. Mater. Sci*. Vol. 27, pp. 5470–5476, 1992.
9. Rhinehart, J. S., and J. Pearson. *Explosive Working of Metals*. New York: MacMillan, pp. 256–257, 1963.
10. Batsanov, S. S. *Effects of Explosions on Materials*. New York: Springer Verlag, p. 49, 1994.
11. Gabriel, K. A., S. G. Wax, and J. W. McCauley (editors). "Materials Processing by Self-Propagating High-Temperature Synthesis (SHS)." *Proceedings of the DARPA/ARMY SHS Symposium*, MTL-SP-87-3, U.S. Government Printing Office, Washington, DC, 1987.
12. Munir, Z. A., and J. B. Holt (editors). *Combustion and Plasma Synthesis of High-Temperature Materials*. New York: VCH Publishers, 1990.
13. Kecskes, L. J., and I. W. Hall. *Metall. Trans. A*. Vol. 26, pp. 2407–2414, 1995.
14. Cullity, B. D. *Elements of X-ray Diffraction*. Second Ed., Reading, MA: Addison-Wesley, chap. 11, pp. 359–360, 1978.

15. Askeland, D. R. *The Science and Engineering of Materials*. Second Ed., Boston: PWS-Kent Company, 1989.

16. Rudy, E., and S. Windisch. *Trans. Metall. Soc. AIME*, vol. 242, pp. 953–954, 1968.

17. Askill, J. *Tracer Diffusion Data for Metals, Alloys, and Simple Oxides*. New York: IFI/Plenum Data Corporation, p. 53, 1970.

18. Williams, B. E., J. J. Stiglich, Jr., and R. B. Kaplan. "Coated Tungsten Powders for Advanced Ordnance Applications, Phase-II SBIR." MTL-TR-92-35, U.S. Army Materials Technology Laboratory, Watertown, MA, May 1992.

19. Williams, B. E., and J. J. Stiglich, Jr. "Hafnium- and Titanium-Coated Tungsten Powders for Kinetic Energy Penetrators, Phase-I SBIR." MTL-TR-92-36, U.S. Army Materials Technology Laboratory, Watertown, MA, May 1992.

20. Raman, R. V. Personal communication. Ceracon, Inc., Sacramento, CA, March 1994.

21. Berning, P. R. "Coating of Tungsten Powder with PVD." TCN 93231, U.S. Army Research Office, Research Triangle Park, NC, November 1993.

22. Dini, J. W. *Tungsten and Tungsten Alloys – 1992*. Edited by A. Bose and R. J. Dowding, Metal Powder Industries Federation, Princeton, NJ, pp. 463–469, 1993.

23. McQuillan, A. D., and M. K. McQuillan. *Titanium*. London: Butterworths Publications, chapter 7, pp. 158–288, 1956.

24. Massalski, T. B., H. Okamoto, P. R. Subramanian, and L. Kacprzak (editors). *Binary Alloy Phase Diagrams*. Second Ed., New York: William W. Scott, 1990.

25. Sandler, S. I. *Chemical and Engineering Thermodynamics*. New York: John Wiley and Sons, pp. 478–480, 1989.

26. Maykuth, D. J., H. R. Ogden, and R. I. Jaffee. *J. Met. Trans. AIME*. Vol. 197, pp. 231-237, 1953.

27. Murray, J. L. *Bull. Alloy Phase Diag*. Vol. 2, pp. 192–196, 1981.

28. Lo, C. F. *Tungsten and Refractory Metals 3 – 1995*. Edited by A. Bose and R. J. Dowding. Princeton, NJ: Metal Powder Industries Federation, pp. 169–181, 1996.

Appendix. Temperature History and Microstructure Evolution of the CSA-HEC Samples

A-1. The Tungsten-Titanium (W-Ti) Phase Diagram

The W-Ti equilibrium phase diagram was shown in Figure 7 of the main report.[1] There are two pertinent features of this system. One is a critical point at 1,250 °C, 33W-67Ti atomic-percent, corresponding to the β-Ti/W ↔ β-Ti + W reaction. The other is the β-Ti/W ↔ W + α-Ti monotectoid reaction at 740 ±20 °C 9W-91Ti atomic-percent. Above the critical temperature (indicative of a miscibility gap), a complete range of bcc β-Ti/W solid solutions exists. The maximum solubility of W in cph α-Ti has been limited to 0.2 atomic-percent. The phase boundaries depicted in the diagram are calculations based on available experimental data.[2,3,4] While the shapes and positions of the liquidus and solidus are in agreement with experimental data, the shape of the miscibility gap, especially for W-rich alloys, is less well known.

A-2. Temperature History the 83W-17Ti Alloy

The results of the auxiliary measurements of the W+Ti powder bed temperature during the preheating phase were essential for the successful consolidation of the W-Ti billets. The experimental data for the n_{TiC}/n_ss of 3.20, 6.29, and 9.07 are presented in Figure A-1. The temperature-time trace for 3.20 appears in Figure A-1(a), for 6.29 in Figure A-1(b), and for 9.07 in Figure A-1(c). Additionally, the temperature-time trace at the interior of the powder bed is shown on an expanded scale in Figure A-1(d). In the lower left-hand corner of each of the plots of Figures A-1(a), A-1(b), and A-1(c), the pair of vertical arrows marks the initiation and completion of the TiC SHS reaction. As expected, with an increasing amount of TiC, the duration of the reaction (i.e., the length of the heat pulse) increases. In all three cases, the temperature at the edge of the

[1] McQuillan, A. D., and M. K. McQuillan. *Titanium*. London: Butterworths Publications, pp. 158–288, 1956.

[2] Nowotny, H., E. Parthe, R. Kieffer, and F. Benesovsky. "The Ternary System Titanium-Tungsten-Carbon." *Z. Metallkunde*. vol. 45, pp. 97–101, 1954.

[3] Rudy, E., and S. Windisch. "Revision of the Titanium-Tungsten System." *Trans. Metall. Soc. AIME* Vol. 242, pp. 953-954, 1968.

[4] Oleynikova, S. V., T. T. Nartova, and I. I. Kornilov. "Examination of the Structure and Properties of Ti-Rich Ti-W Alloys." *Russ. Metall.*, vol. 3, pp. 130–133, 1971.

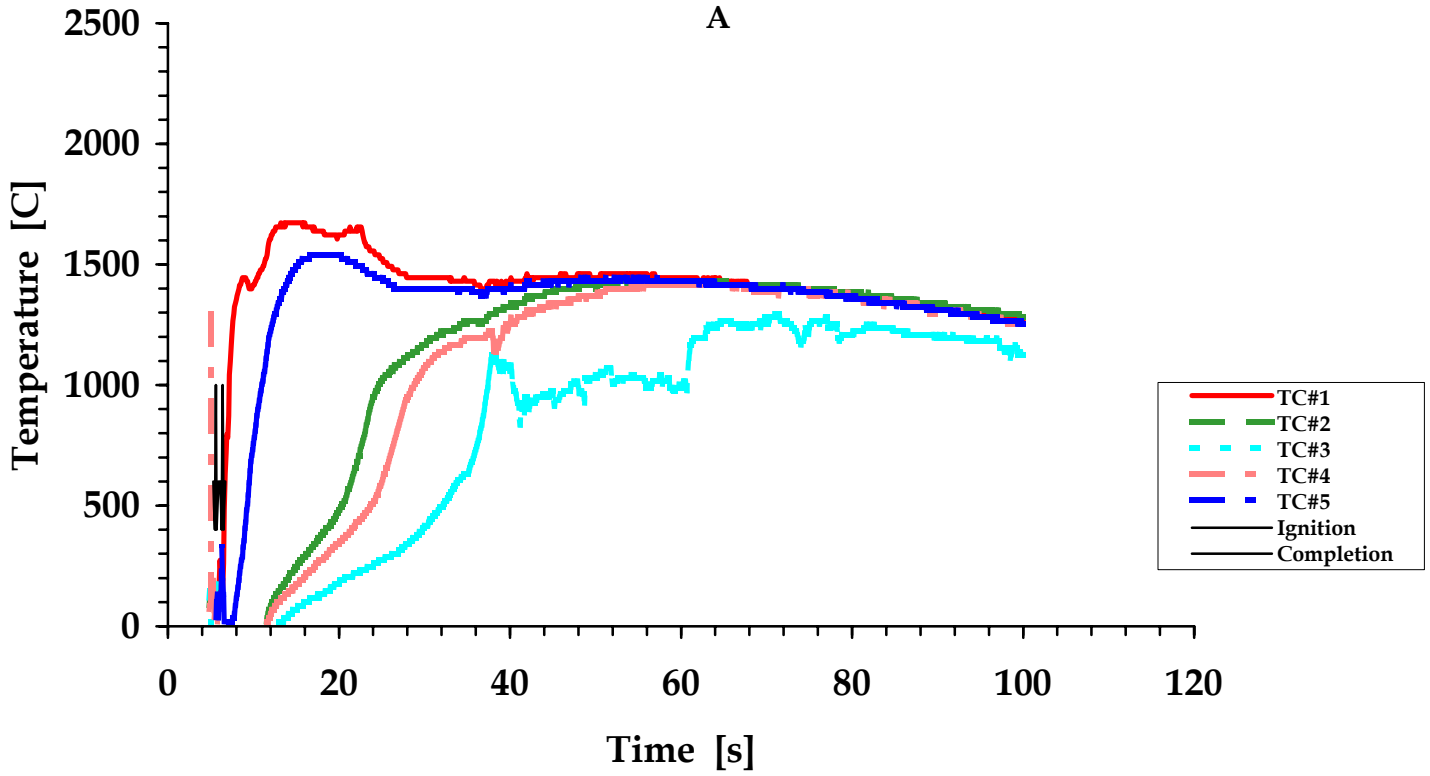

(a) Temperature data for the 83W-17 Ti powder bed with an $n_{TiC}/n_s = 3.20$.

Figure A-1. Temperature data for the 83W-17Ti powder bed with an $n_{TiC}/n_s = 3.20$ is shown in (a), $n_{TiC}/n_s = 6.29$ is shown in (b), $n_{TiC}/n_s = 9.07$ is shown in (c), and interior temperature for all three n_{TiC}/n_ss is shown in (d).

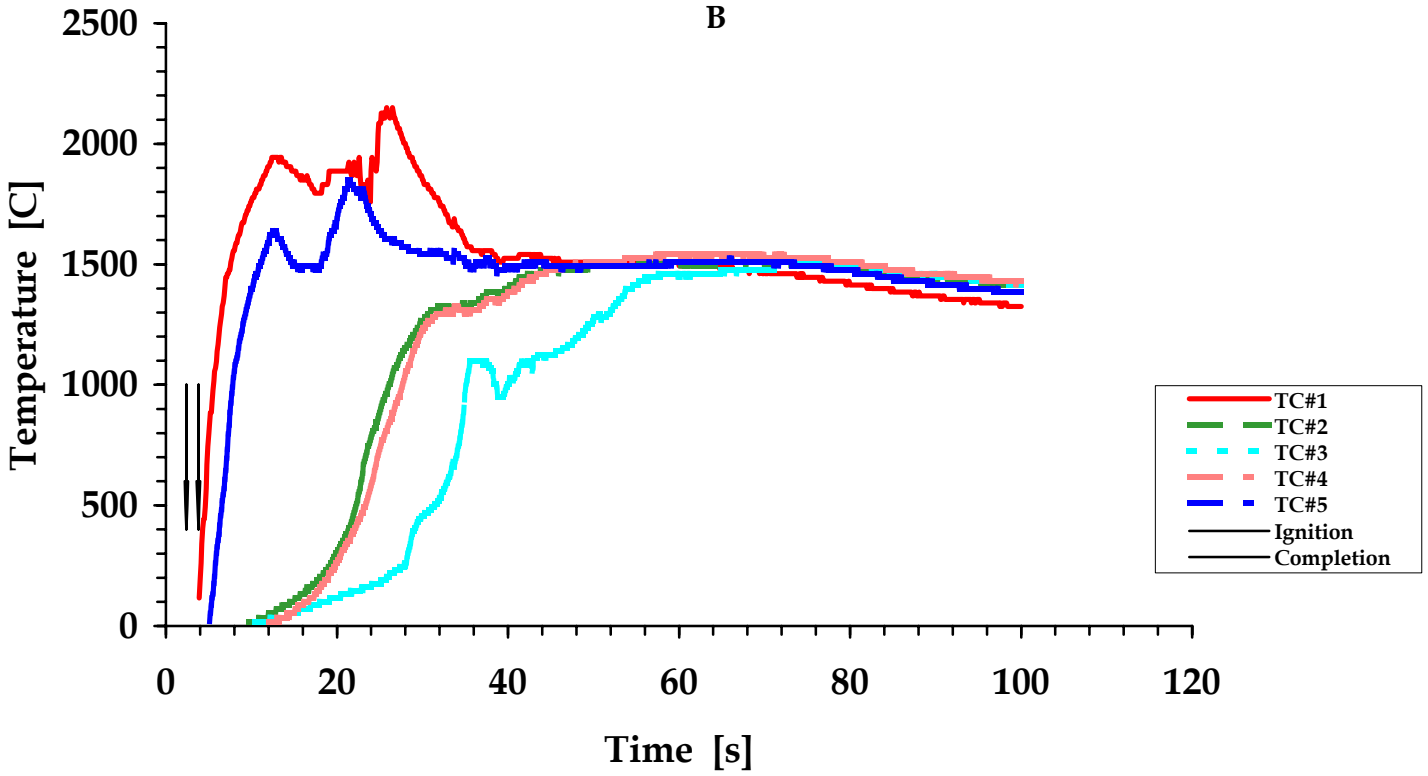

(b) Temperature data for the 83W-17Ti powder bed with an $n_{TiC}/n_s = 6.29$.

Figure A-1. Temperature data for the 83W-17Ti powder bed with an $n_{TiC}/n_s = 3.20$ is shown in (a), $n_{TiC}/n_s = 6.29$ is shown in (b), $n_{TiC}/n_s = 9.07$ is shown in (c), and interior temperature for all three n_{TiC}/n_ss is shown in (d) (continued).

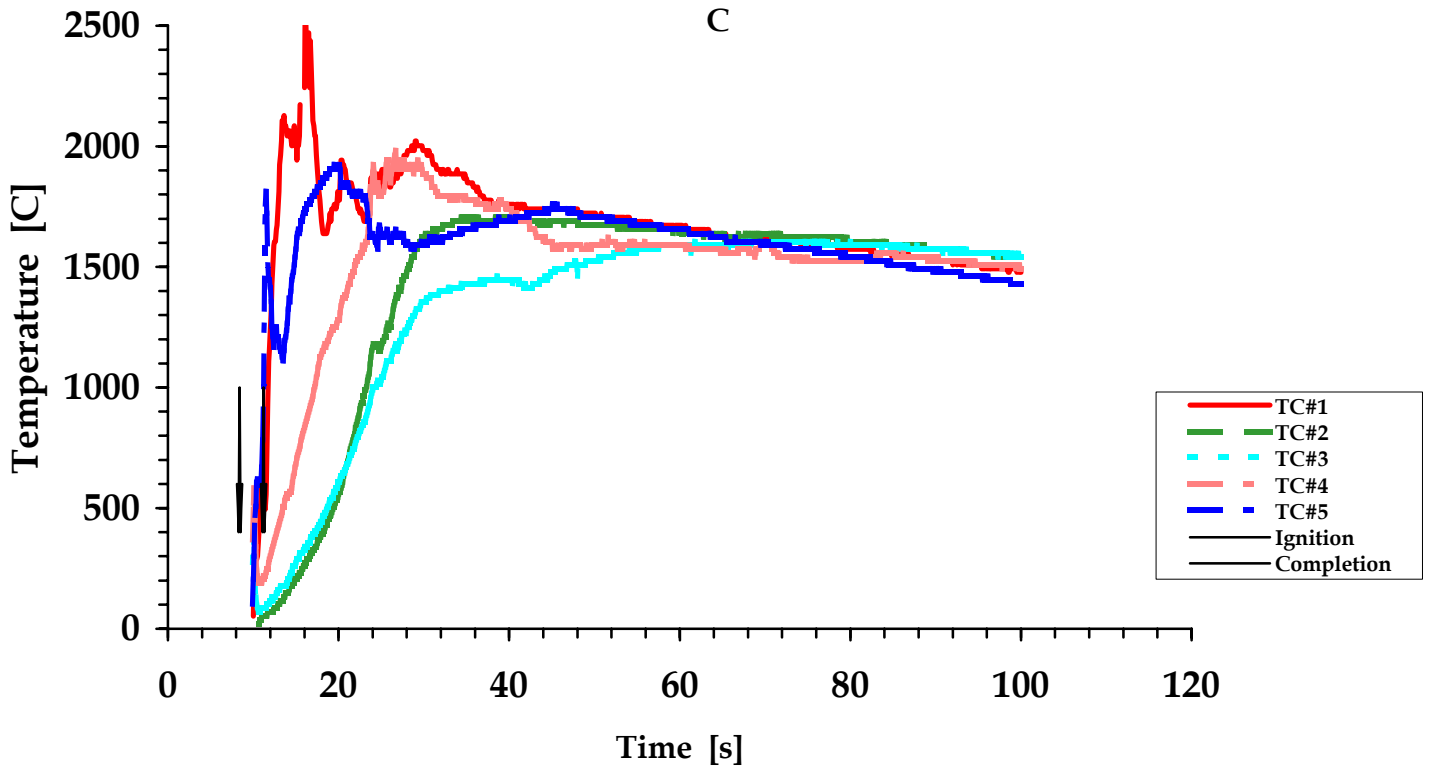

(c) Temperature data for the 83W-17Ti powder bed with an $n_{TiC}/n_s = 9.07$.

Figure A-1. Temperature data for the 83W-17Ti powder bed with an $n_{TiC}/n_s = 3.20$ is shown in (a), $n_{TiC}/n_s = 6.29$ is shown in (b), $n_{TiC}/n_s = 9.07$ is shown in (c), and interior temperature for all three n_{TiC}/n_ss is shown in (d) (continued).

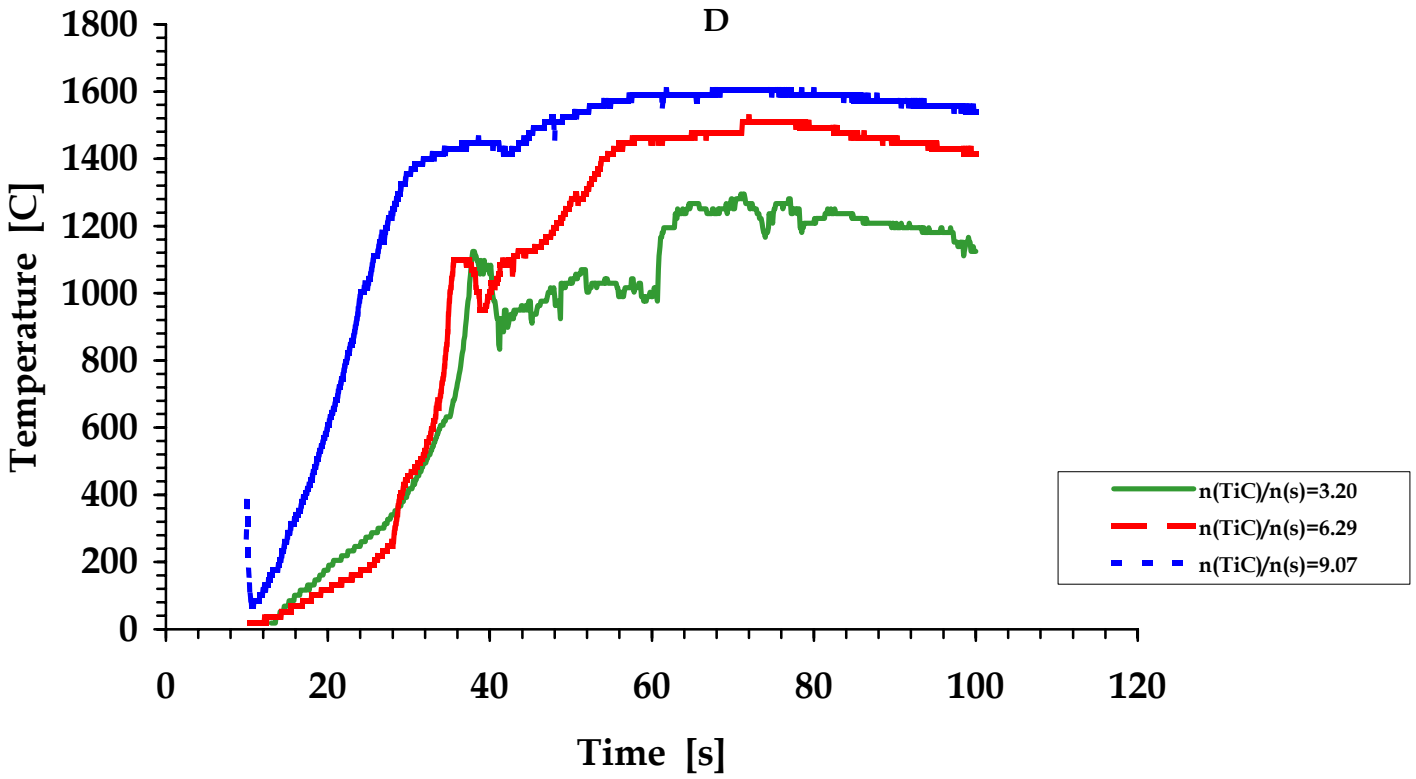

(d) Temperature data for the 83W-17Ti powder bed with an interior temperature for all three n_{TiC}/n_ss.

Figure A-1. Temperature data for the 83W-17Ti powder bed with an n_{TiC}/n_s = 3.20 is shown in (a), n_{TiC}/n_s = 6.29 is shown in (b), n_{TiC}/n_s = 9.07 is shown in (c), and interior temperature for all three n_{TiC}/n_ss is shown in (d) (continued).

powder beds rises rapidly to reach a broad peak, drops, goes through a plateau, and then (due to continued heat losses) steadily decreases. As the heat pulse travels inward to the sample center, the temperature profile is changed. A more sluggish rise in the temperature and the absence of the peak result in a wide plateau and subsequent decline only. Thus, an immediate conclusion from the data is that the periphery of the powder bed undergoes a different thermal history than the midregions.

As seen in Figure A-1(a), for n_{TiC}/n_s = 3.20 the peak temperature is 1,500 °C at one end of the powder bed and is near the melting point of Ti at the other (T_m Ti = 1,670 °C). The temperature at the powder bed's center is only 1,250 °C, well below T_m Ti. For n_{TiC}/n_s = 6.29, the temperature at the outer edge of the powder bed reaches 1,900 °C at one end and 2,100 °C at the other (see Figure A-1[b]). In this case, the powder bed's center temperature is higher, reaching 1,550 °C, but does not exceed T_m Ti. Finally, in Figure A-1(c), for n_{TiC}/n_s = 9.07 the powder bed reaches temperatures well above 2,400 °C at its periphery and 1,650 °C at its center. Although the heating rates (note the temperature rise in the curves) for the two smaller n_{TiC}/n_ss are similar, in the n_{TiC}/n_s = 9.07 case it is markedly different. Specifically, the temperature rise at the powder bed interior is more rapid, much like that of the periphery. In the two cases with larger n_{TiC}/n_ss, the critical aspect of the data is that at approximately 60 s after the initiation of the TiC reaction, the W+Ti powder bed becomes isothermal. In the case with n_{TiC}/n_s = 3.20, the powder bed never reaches an isothermal plateau and continues to undergo severe temperature gradients.

The temperature-time data presented previously reveal that the n_{TiC}/n_s significantly affects the heating rates and peak temperatures attained within the W+Ti powder bed. Even at the smallest n_{TiC}/n_s, the temperature at the sample edge nearly reaches T_m Ti. A threefold increase of n_{TiC}/n_s results in a 1,000 °C increase in the powder bed edge temperature. The powder bed's center is less sensitive to this change, since the interior temperature varies only by about 400 °C (see Figure A-1[d]). Ideally, for best compaction results, the n_{TiC}/n_s should be adjusted so that as much as possible of the bulk of the powder bed is near (but does not exceed) the T_m Ti, and excessive overheating of the periphery is minimized. However, unless a large enough n_{TiC}/n_s is used, the W+Ti sample will not become isothermal at any point during the preheating cycle. The n_{TiC}/n_s of about 6.3 satisfies both of these criteria.

A-3. Microstructure of the 83W-17Ti Alloy

Optical microscopy of transverse (perpendicular) and longitudinal (parallel) cross sections (with respect to the compaction axis) revealed a preferentially oriented two-phase structure. The distribution of the primary W (gray) and secondary Ti-rich (black) phases is isotropic in the transverse view; however, both phases tend to be elongated along a transverse plane in the longitudinal

view. This appearance is consistent with stage-two compaction wherein grains deform plastically without exceeding the breaking stress in the powder body. EDS analysis of the samples showed that the primary phase consists of W only, and the secondary matrix phase is a Ti-rich β-Ti/W solid solution. During the course of these analyses, no other elements were identified in the W-Ti billets.

Polished, longitudinal cross sections from the core, transition (intermediate), and edge regions are shown in Figures A-2(a), A-2(b) and A-2(c) for a typical sample. As seen in Figure A-2(a), the BSE-COMP micrograph of the core region of the billet reveals a structure consisting of loose W grain aggregates (light gray) bounded by a partially continuous Ti-rich β-Ti/W matrix (dark gray to black). The dimensions of the matrix region roughly correspond to those of the precursor Ti particles. The extent of the billet core comprises a disk with a radius of about 19–20 mm. As indicated by arrows in Figure A-2(a), in some instances the Ti-rich phase is found to extend into the W aggregates. The matrix contains an equiaxed grain structure with an average size of 5–10 μm.

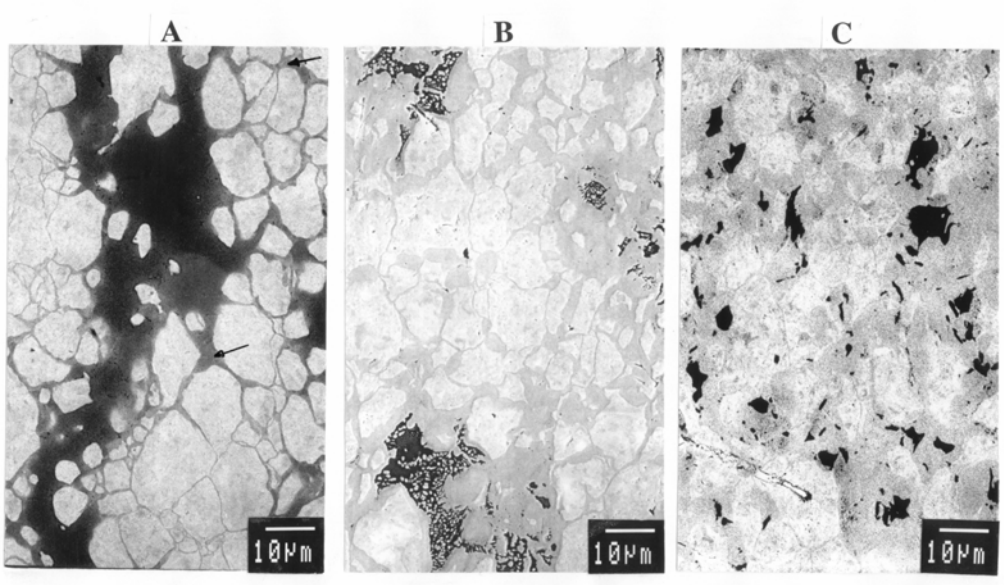

Figure A-2. BSE-COMP micrographs of polished surfaces of a typical 83W-17Ti billet. Core region is shown in (a), transition region is shown in (b), and edge region is shown in (c).

Using EDS analysis, the W grains contained in the aggregates had a W content over 99 atomic-percent. The Ti-rich β-Ti/W phase had a composition range of about 25W-75Ti to 20W-80Ti. The usual compositional uniformity of the matrix was about 5 atomic-percent. This is consistent with the high diffusivity of W in β-Ti at the precompaction temperatures ($D = 8.2 \times 10^{-9}$ cm^2/s).[5] In regions where

[5] Askill, J. *Tracer Diffusion Data for Metals, Alloys, and Simple Oxides.* New York: IFI/Plenum Data Corporation, p. 53, 1970.

the matrix was closely bounded by W grains, the Ti content was lower by about 10 atomic-percent than the overall matrix composition. Typically, the W:Ti ratio dropped rapidly within a few micrometers from the W grain edge to its average level at the center of the matrix.

The micrograph from the intermediate region of the billet (see Figure A-2[b]) reflects a significant shift from this morphology caused by higher local temperatures of about 1,800 °C. This annular region surrounding the core is approximately 4–8 mm inward from the edge of the billet. Unlike the relative homogeneity of each phase observed earlier, as seen in Figure A-2(b), intermixing W and Ti is more extensive and heterogeneous. The intensified dissolution of W grains can be noted in the appearance of a continuous, 3- to 5 μm-wide, W-rich β-Ti/W solid solution surrounding W grain remnants. Observed mainly in the Ti-rich β-Ti/W matrix phase, examples of heterogeneous, nonequilibrium partitioning include submicrometer-sized precipitate clusters, micrometer-sized grain-boundary precipitates, and monotectoid duplex structures. EDS results showed 25W-75Ti to 30W-70Ti for the Ti-rich β-Ti/W phase and 60W-40Ti to 70W-30Ti for the W-rich β-Ti/W phase. Closer examination of the immediate vicinity surrounding precipitates showed 50W-50Ti for the precipitates and 25W-75Ti for the adjacent Ti-rich region.

Lastly, the edge region, or the outer 4-mm annulus, of the billet (see Figures A-2[c]) exhibits the thermally most active state between the two components. It may be recalled that the temperature at the billet edge was near or above 2,000 °C. In this region, the original W grains have mostly dissolved to form an interconnected W-rich solid solution, leaving the Ti-rich phase in small, (5–15 μm) isolated islands. EDS of this region revealed about 75W-25Ti for W-rich β-Ti/W areas and 5W-95Ti for the Ti-rich β-Ti/W islands. It may be noted that in the latter figures the W grains and Ti-rich regions have much straighter edges, indicating plastic shear deformation as well.

A-3.1. Morphological Evolution

The nonuniform distribution of Ti in the alloy billet is probably brought about by the considerable particle size difference, the relative melting points of the precursors, and the temperature at the time of compaction. At temperatures below T_m Ti = 1,670 °C in the core region, the Ti, though moderately plastic, is unable to flow extensively and cannot spread uniformly between all of the W grains. With sample temperatures exceeding T_m Ti, the ability of Ti to spread beyond the nearby W aggregates increases, causing their dispersion and breakup, thereby creating more uniformity and continuity in the matrix surrounding the W particles. However, the added effect of the increased mobility of the Ti causes an associated rise in the degree of intermixing between the W and Ti components in the matrix itself and at the W grain/β-Ti/W matrix interface.

The intermixing of the W and Ti may not be detrimental to the alloy, but it is very likely that unless the affected regions could be avoided or eliminated, segregation and heterogeneity of the sample microstructure will result in nonuniform properties. The pronounced shift in morphologies can be understood by carefully examining the heating and cooling cycle of each region of the 83W-17Ti alloy. A possible explanation of the observed microstructures is offered hereafter.

During the preheating phase, the temperature of the outer edge (~2,000–2,200 °C) of the billet rapidly rises well above the solidus. With a sufficiently prolonged exposure (60 s) at these temperatures in the two-phase (liquid+solid) region, the W grains dissolve into solution, and the composition shifts toward the W-rich side (60W-40Ti) of the miscibility gap in the phase diagram (see Figure 7 in the main report and Figure A-1[b]). Note that with the rapid heating conditions present, the equilibrium phase diagram can only be used as a guide to interpret "equilibrium-like" conditions. During the delay time, cooling of the region below the solidus has begun; nevertheless, the combination of two factors could enhance further shifting past the miscibility gap to the W-rich end 75W-25Ti of the phase diagram. These factors are the additional temperature rise during the irreversible work of consolidation in the sample, and the presence of the nearby, still relatively hot, TiC. Slow cooling adjacent to the TiC will maintain near-equilibrium conditions that could permit the allowed phase separation beyond the miscibility gap.

The heating of the transition region is not as rapid; however, the temperature (~1,800 °C) also crosses the solidus. Consequently, prior to consolidation, the β-Ti/W solid solution may only reach a hypermonotectoid, 35W-65Ti composition within the miscibility gap. The cooling in this region is generally not rapid enough to completely quench in this metastable solid solution. It is sufficiently slow to allow partial phase separation within short, micrometer-length distances. In certain areas, when the combination of local heat content and cooling rate permit, the initial hypermonotectoid composition to dissociate (i.e., travel along the opposite sides of the miscibility gap solvus) typical monotectoid structures can result.

Finally, in the core region, W, heated gradually to the isothermal plateau to a temperature of 1,550 °C (still below T_m Ti), dissolves in Ti to form a Ti-rich β-Ti/W solid solution of 25W-75Ti. In spite of the heat added during consolidation, this region is quenched quickly ($\partial T/\partial t$ = ~10^2 to 10^3 °C/s) as heat is conducted out directly, unimpeded, into the steel fixture through the densified ZrO_2 thermal insulation and steel anvil inserts.

A comparison of the W:Ti ratios in the precompacted and compacted structures indicates that the heat, added from the irreversible work and proximity of the TiC, does not shift the preconsolidation compositions toward the W-rich end of the phase diagram. In other words, the effect of the compaction process is

limited to the closure of porosity from a loosely connected (i.e., distended) network of "preformed" building blocks. Interparticle frictional heat that may be generated is most likely dissipated and conducted out of the compacted body through the densified medium. Likewise, the composition-modifying effect of the hot TiC is restricted to the outer 5- to 6-mm periphery and has no role in the interior transition and core regions. It may be also deduced that the near "equilibrium-like" condition exists during the preheating phase only. The composition of the CSA-HEC alloys is unaffected by any heating that may take place during the consolidation process.

A-3.2. Microstructural Changes With n_{TiC}/n_s

The microstructures of the precompacted sponges and CSA-HEC samples fabricated using higher and lower n_{TiC}/n_ss differed only in the location and width of the morphological transition zones. Since the initial heat pulse appeared to affect only the peak temperatures attained in the fixture, it was concluded that all samples in the CSA-HEC fixture, regardless of the n_{TiC}/n_s, undergo similar precompaction thermal histories.

SEM examination of the CSA-HEC billets revealed a generally similar, oriented structure. At the lower ratio (3.23), the Ti-rich β-Ti/W matrix phase was more oriented and practically discontinuous in the core. A fine, submicrometer-sized porosity that was absent in the standard sample (n_{TiC}/n_s = 6.44) appeared between matrix subgrains. EDS analysis of the Ti-rich phase indicated Ti contents slightly higher (by about 5 atomic-percent) than those of the standard billet. The morphological transition regions, as described previously, existed from the edge to the core of this billet. However, their extent was spatially narrower and located closer to the billet's edge.

At the higher ratio (8.32), the W aggregate breakup in the sample was more extensive, resulting in the improvement of Ti-rich matrix's continuity. With an improvement of the dispersion, the orientation effect was somewhat reduced. Additionally, because of the higher interior temperatures in this case, the morphological transition from the edge of the sample to its core was wider, and the corresponding regions were located further inward, toward the billet's center. The Ti content in the matrix was about the same as that found in the standard billet.

NO. OF COPIES ORGANIZATION

2 DEFENSE TECHNICAL INFORMATION CENTER
DTIC OCA
8725 JOHN J KINGMAN RD
STE 0944
FT BELVOIR VA 22060-6218

1 HQDA
DAMO FDT
400 ARMY PENTAGON
WASHINGTON DC 20310-0460

1 OSD
OUSD(A&T)/ODDR&E(R)
DR R J TREW
3800 DEFENSE PENTAGON
WASHINGTON DC 20301-3800

1 COMMANDING GENERAL
US ARMY MATERIEL CMD
AMCRDA TF
5001 EISENHOWER AVE
ALEXANDRIA VA 22333-0001

1 INST FOR ADVNCD TCHNLGY
THE UNIV OF TEXAS AT AUSTIN
3925 W BRAKER LN STE 400
AUSTIN TX 78759-5316

1 US MILITARY ACADEMY
MATH SCI CTR EXCELLENCE
MADN MATH
THAYER HALL
WEST POINT NY 10996-1786

1 DIRECTOR
US ARMY RESEARCH LAB
AMSRL D
DR D SMITH
2800 POWDER MILL RD
ADELPHI MD 20783-1197

1 DIRECTOR
US ARMY RESEARCH LAB
AMSRL CI AI R
2800 POWDER MILL RD
ADELPHI MD 20783-1197

NO. OF COPIES ORGANIZATION

3 DIRECTOR
US ARMY RESEARCH LAB
AMSRL CI LL
2800 POWDER MILL RD
ADELPHI MD 20783-1197

3 DIRECTOR
US ARMY RESEARCH LAB
AMSRL CI IS T
2800 POWDER MILL RD
ADELPHI MD 20783-1197

ABERDEEN PROVING GROUND

2 DIR USARL
AMSRL CI LP (BLDG 305)

NO. OF COPIES ORGANIZATION

4 COMMANDER
US ARMY RESEARCH OFFICE
I AHMAD
E CHEN
A CROWSON
R REEBER
PO BOX 12211
RESEARCH TRIANGLE PARK NC 27709-2211

1 DIRECTOR
BENET WEAPONS LAB
SMCAR CCB TL
W KITCHENS JR
WATERVLIET NY 12189

1 COMMANDER
USA AMCCOM
SMCAR ESP L
ROCK ISLAND IL 61299

2 COMMANDER
USA FOREIGN SCIENCE
AND TECHNICAL CENTER
J CRIDER
W MARLEY
220 SEVENTH ST NE
CHARLOTTESVILLE VA 22901

1 COMMANDER
DARPA
P PARRISH
3701 N FAIRFAX DR
ARLINGTON VA 22203-1714

1 AIRTRON DIVISION
J INGS
200 EAST HANOVER AVE
MORRIS PLANES NJ 07950

3 GEORGIA INST OF TECH
K LOGAN
N THADHANI
J WALTON
778 ATLANTIC DRIVE
ATLANTA GA 30332

3 IDAHO NATIONAL ENG LAB
B RABIN
G KORTH
R WRIGHT
PO BOX 1625
IDAHO FALLS ID 83415

NO. OF COPIES ORGANIZATION

2 SOUTH DAKOTA SCHOOL OF
MINES AND TECHNOLOGY
CHEMISTRY AND CHEMICAL
ENGINEERING DEPARTMENT
J PUSZYNSKI
F MARQUIS
501 E ST JOSEPH STREET
RAPID CITY SD 57701

1 UNIV OF CA SAN DIEGO
INST OF MECHS OF MTRLS
M MEYERS
9500 GILMAN DRIVE
LA JOLLA CA 92093

ABERDEEN PROVING GROUND

36 DIR USARL
AMSRL WM
J SMITH
D ECCLESHALL
G KLEM
AMSRL WM T
P BERNING
W BRUCHEY
B BURNS
K FRANK
P KINGMAN
L MAGNESS
A NIILER
E RAPACKI
W WALTERS
T WEERASOORIYA
AMSRL WM M
R ADLER
K ANDERSON
J BEATTY
E CHIN
K CHO
W DEROSSET
R DOWDING
B FINK
L KECSKES (10 CPS)
J LASALVIA
W ROY
R SHUFORD
D SNOHA
M STAKER

REPORT DOCUMENTATION PAGE

Form Approved
OMB No. 0704-0188

1. AGENCY USE ONLY *(Leave blank)*	2. REPORT DATE	3. REPORT TYPE AND DATES COVERED
	November 2001	Final, January 1992–December 1997

4. TITLE AND SUBTITLE
Hot Explosive Consolidation of W-Ti Alloys: Microstructural Effects

5. FUNDING NUMBERS
IL622105AH84–622195A

6. AUTHOR(S)
Laszlo J. Kecskes

7. PERFORMING ORGANIZATION NAME(S) AND ADDRESS(ES)
U.S. Army Research Laboratory
ATTN: AMSRL-WM-MD
Aberdeen Proving Ground, MD 21005-5069

8. PERFORMING ORGANIZATION REPORT NUMBER
ARL-TR-2615

9. SPONSORING/MONITORING AGENCY NAMES(S) AND ADDRESS(ES)

10. SPONSORING/MONITORING AGENCY REPORT NUMBER

11. SUPPLEMENTARY NOTES

12a. DISTRIBUTION/AVAILABILITY STATEMENT
Approved for public release; distribution is unlimited.

12b. DISTRIBUTION CODE

13. ABSTRACT *(Maximum 200 words)*

Full-density W-Ti alloys have been fabricated by a recently developed, hot-explosive-compaction (HEC) technique. The alloy billets, which are formed, consist of W grains embedded in a generally discontinuous, preferentially oriented Ti-rich matrix. The effects of the use of different types of precursor powders, the influence of the W-Ti ratio on the dispersability of the W grains in the alloy, and the postconsolidation anneal control of the Ti-rich matrix were of primary interest. The alloy billets were analyzed by X-ray diffraction (XRD), scanning electron microscopy (SEM), and energy dispersive spectroscopy (EDS). The major features of the technique and the microstructural properties of the W-Ti alloys are presented.

14. SUBJECT TERMS	15. NUMBER OF PAGES
hot explosive consolidation, W-Ti alloy microstructure, properties, processing-structure	48
	16. PRICE CODE

17. SECURITY CLASSIFICATION OF REPORT	18. SECURITY CLASSIFICATION OF THIS PAGE	19. SECURITY CLASSIFICATION OF ABSTRACT	20. LIMITATION OF ABSTRACT
UNCLASSIFIED	UNCLASSIFIED	UNCLASSIFIED	UL

NSN 7540-01-280-5500

Standard Form 298 (Rev. 2-89)
Prescribed by ANSI Std. 239-18 298-102